

**A NUMERICAL AND EXPERIMENTAL STUDY
FOR RESIDUAL STRESS EVOLUTION IN LOW
ALLOY STEEL DURING LASER AIDED ADDITIVE
MANUFACTURING PROCESS**

by

Hyung Min Chae

A dissertation submitted in partial fulfillment
of the requirements for the degree of
Doctor of Philosophy
(Mechanical Engineering)
in the University of Michigan
2013

Doctoral Committee:

Professor Jyotirmoy Mazumder, Chair
Associate Professor Vikram Gavini
Professor Jwo Pan
Professor Anthony M. Waas

Rejoice in the Lord always. I will say it again: Rejoice!
Let your gentleness be evident to all. The Lord is near.
Do not be anxious about anything, but in everything, by prayer and petition,
with thanksgiving, present your requests to God.
And the peace of God, which transcends all understanding,
will guard your hearts and your minds in Christ Jesus.

Philippians 4:4-7

© Hyung Min Chae 2013

To my parents

ACNOWLEDGEMENTS

I would like to express my sincerest thanks to those who helped me pursuing and completing my Ph.D at the University of Michigan.

First of all, my sincere gratitude goes to my advisor, Professor Jyotirmoy Mazumder. He has instructed me with his ingenious insights and endless passions throughout my Ph.D study. His valuable guidance has built me as a professional engineer, improved my project management and technical communication skills, and influenced of which on my personal development will be forwarded into my future career. I really appreciate to my dissertation committee, Professor Vikram Gavini, Professor Jwo Pan, and Professor Anthony M. Waas for serving on the committee and improving the dissertation with critiques and insights. My thanks go out to NSF/IUCRC and Focus Hope for financial supports for the research. I would also like to thank to Mr. Frederick Dunbar and Mr. William Johnson for the help at the CLAIM research group.

Lastly, I would like to express thank to my parents. Without their continuous and unconditional support, love, trust, and encouragement throughout my life, this study could not be completed.

TABLE OF CONTENTS

DEDICATION	ii
ACNOWLEDGEMENTS	iii
LIST OF FIGURES	vi
LIST OF TABLES	x
NOMENCLATURE	xi
ABSTRACT	xvi
CHAPTER	
I. INTRODUCTION	1
II. NUMERICAL MODELING: THERMAL MODEL	7
2.1 Introduction	7
2.2 Assumptions	8
2.3 Boundary conditions / Governing equation / Flow chart	9
2.4 Non-equilibrium partitioning in solidification	24
2.5 Numerical results	27
2.5.1 Laser powder interaction	27
2.5.2 Temperature / fluid flow / solute transport	31
2.5.3 Effects of processing parameters on deposition geometry	37
2.6 Experimental validations	38
2.6.1 Evolution of temperature and fluid flow	38

2.6.2 Geometry changes with processing parameter	41
2.7 Conclusions	42
III. NUMERICAL MODELING: MECHANICAL DEFORMATION MODEL	45
3.1 Introduction	45
3.2 Assumptions	46
3.3 Boundary conditions / Constitutive model / Flow chart	46
3.4 Martensitic phase transformation in laser material processing	52
3.5 Evolution of residual stress in DMD process	57
3.6 Effects of volumetric dilatation due to martensite phase transformation	63
3.7 Experimental validations: X-ray diffraction residual stress measurement	66
3.8 Conclusions	68
IV. CORRELATIONS OF PROCESSING CONDITIONS	70
4.1 Introduction	70
4.2 Metallic powder flow rate	71
4.3 Laser power	74
4.4 Scanning speed	76
4.5 Scanning direction / deposition layer thickness	78
4.6 Conclusions	83
V. CONTRIBUTIONS AND FUTURE WORKS	85
5.1 Contributions	85
5.2 Future works	87
BIBLIOGRAPHY	90

LIST OF FIGURES

FIGURE

1.1	Direct Metal Deposition (DMD) process with feedback sensors	6
2.1	Numerical simulation domain: plane symmetric ($Y=0$) with non-uniform mesh for minimal computational cost	11
2.2	Thermo-physical material properties of AISI 4340 steel: (a) Thermal conductivity (b) Specific heat [24]	14
2.3	A sinusoidal function, used to smooth out the significant difference in material properties across the liquid / gas interface, guarantees the full convergence during computation	15
2.4	Boundary conditions used in the DMD thermal model	17
2.5	Temperature dependent absorption coefficient of AISI 4340 steel with DISC laser	18
2.6	Flow chart of thermal model in DMD process	22
2.7	Schematic drawing of narrow band level-set method	24
2.8	Geometric model for solid / liquid interface at mushy zone during solidification in laser material processing [33]	26
2.9	Dynamic non-equilibrium phase diagram of binary carbon-iron system	26
2.10	Laser intensity profile with various laser mode, TEM_{00} , TEM_{01}^* , and Top hat mode	29
2.11	Powder temperature profile at the substrate with TEM_{01}^* -CO2 laser	29

2.12	(a) Powder temperature (b) the number of powdered particles along the Z axis with TEM ₀₀ -CO ₂ laser	30
2.13	Powder temperature along the Z axis with Top hat-CO ₂ laser	31
2.14	Temperature field and fluid flow in DMD process (cross sectional view of X-Z plane with 1mm-Top hat-CW-DISC laser)	32
2.15	Temperature field and fluid flow in DMD process (cross sectional view of Y-Z plane with 2mm-TEM ₀₁ *-CW-CO ₂ laser)	33
2.16	Maximum temperature of the melt pool with different laser power range from 1400 to 2300 Watts (1 mm TEM ₀₀ -CW-CO ₂ laser)	34
2.17	Mathematically predicted cooling rates at different locations in DMD process	35
2.18	Solute transport in the laser melted pool of AISI 4340 steel: The Pectlet number for Carbon: 3.15E4 and for Nickel:1.69E5, Advective transport >> Diffusion transport	36
2.19	Melt pool geometry changes with processing conditions	37
2.20	Numerically and experimentally obtained temperature history of the DMD fabricated material. The locations (a)~(d) are shown in Figure 2.17	39
2.21	Successive images of melt pool in DMD process taken by a high speed CCD camara	40
2.22	Experimental validation of melt pool geometry (width, height, and penetration to the substrate) with different laser power	41
3.1	Stress state correction using radial return method	48
3.2	Temperature dependent coefficient of themal expansion (CTE) for AISI 4340 steel [24]	50
3.3	Flow chart of mechanical deformation model in DMD process	51
3.4	Martensite is found in AISI 4340 steel deposition using 1.0 mm-Top hat-CW-DISC laser: (a) Top (b) Middle (c) Bottom region of a single layer deposition	54

3.5	Numerically calculated volume fraction of metallurgical phases (Martensite and Perlite) at different locations with 1.0 mm-Top hat-CW-DISC laser	56
3.6	Transient (a) and residual stress (b) in longitudinal (beam scanning) direction of a single AISI 4340 steel layer deposition	59
3.7	Transient (a) and residual stress (b) in transverse direction of a single AISI 4340 steel layer deposition	60
3.8	Evolution of residual stress with temperature: (a) above the melt pool interface (b) below the interface	62
3.9	Martensite phase transformation effects on the residual stress profile along the Z axis (the dashed down arrow in Figure 2.17 shows the region where the residual stress profile is made) Note that S_{xx}^* is the averaged residual stress within the deposition width.	64
3.10	Evolution of S_{xx} stress component near the melt pool interface with and without martensite phase transformation: (a) above the interface (b) below the interface	65
4.1	Residual stresses along the Z axis with different powder flow rate (4.7 g/min to 6.3 g/min): (a) S_{xx} component (b) S_{yy} component (c) S_{zz} component (the dashed down arrow in Figure 2.17 shows the region where the residual stress profile is made)	73
4.2	Residual stresses along the Z axis with different laser power (600 Watt to 800 Watt): (a) S_{xx} component (b) S_{yy} component (c) S_{zz} component (the dashed down arrow in Figure 2.17 shows the region where the residual stress profile is made)	75
4.3	Residual stresses along the Z axis with different laser scanning speed (8.5 mm/s to 12.8 mm/s): (a) S_{xx} component (b) S_{yy} component (c) S_{zz} component (the dashed down arrow in Figure 2.17 shows the region where the residual stress profile is made)	77
4.4	Different scanning techniques to investigate the effects of scanning direction and deposition layer thickness on the residual stress (target deposition height of 300 microns)	78
4.5	Temperature history of double layer deposition with different scanning directions	80

4.6	Residual stresses along the Z axis with different scanning direction and layer thickness (See Figure 4.4): (a) S_{xx} component (b) S_{yy} component (c) S_{zz} component (the dashed down arrow in Figure 2.17 shows the region where the residual stress profile is made)	81
4.7	Transient stress with the different number of scanings in 300 micron height deposition of AISI 4340 steel: (a) tensile region (close to the melt pool interface) (b) compressive region (600 micron below the interface) after the first layer deposition	82
5.1	Zigzag pattern laser scanning for a single block fabrication	88
5.2	Different scanning direction in laser aided metal deposition of a block with a hole: (a) circular scanning (b) one by one scanning	89

LIST OF TABLES

TABLE

2.1	Temperature dependent electrical resistivity of AISI 4340 steel	11
2.2	Elemental composition of AISI 4340 steel [18]	12
2.3	Material properties of AISI 4340 steel used in thermal analyses	13
2.4	Source term at the liquid / vapor interface in each governing equation	21
3.1	Plastic behavior of AISI 4340 steel: Johnson-Cook hardening model [36]	47
3.2	Longitudinal (S_{xx}) residual stresses of a single DMD layer of AISI 4340 steel	67

NOMENCLATURE

Greek letters

α	thermal expansion coefficient
β	dimensionless solidification rate
γ	austenite
Γ	material constant
δ_{ij}	Dirac delta function
Δ	a finite increment
$\Delta\varepsilon$	total strain change in a time step
ε	smoothing thickness
ε_m	emissivity
$\bar{\varepsilon}_p$	effective plastic strain
$\dot{\varepsilon}$	effective strain rate
$\dot{\varepsilon}_0$	reference effective strain rate
ε^{th}	thermal strain
ε^V	volumetric dilatation due to phase transformation
ε^{tp}	phase transformation induced plastic strain
ε^e	elastic strain
ε^p	plastic strain
η	absorption coefficient

κ	curvature
Λ	material constant
λ	wavelength
λ_L	Lamé parameters
μ	viscosity
Π	material constant
ρ	density
σ	Stefan–Boltzmann constant
σ_{ij}	stress in tensor form
σ_e	effective stress
σ_Y	flow stress
φ	the state of the matter (liquid or gas)
ϕ	Von Mises yield surface
Φ	liquid / vapor interface

Latin letters

a	mushy zone dimension
A	area
b	mushy zone dimension
c	constant
C	solute content (in wt%)
C_{conv}	convection heat transfer coefficient
C_p	heat capacity
C_{Li}	liquid solute concentration at the solid liquid interface

C_{Lo}	initial solute concentration at the liquidus line
C_L^*	liquidus composition from equilibrium phase diagram
C_S^*	solidus composition from equilibrium phase diagram
$CR1$	cooling rate from melting temperature to austenite temperature
$CR2$	cooling rate from austenite temperature to martensite start temperature
D	diffusion coefficient
D_{ABs}	inter-diffusion coefficient of species A with respect to species B
e_i	unit vector in i component
f	volume fraction
f^*	fictitious volume fraction
F	force function (speed function)
F_{adv}	advection speed
F_{curv}	curvature force
$Flow_P$	powder flow rate
G	shear modulus
h	enthalpy
H	smoothing function
k	thermal conductivity
k_{ne}	non-equilibrium partitioning coefficient
k_e	equilibrium partitioning coefficient
K	isotropic permeability
l	powder travel distance
L	characteristic length

L_m	heat of fusion
M_s	martensite start temperature
M_f	martensite finish temperature
n	material constant
N	the number of powder density
m	material constant
p	pressure
pr	material property
Pe	Pectlet number
q	laser beam intensity
q'	attenuated laser beam intensity
r	radial distance
R	ideal gas constant
R_E	electrical resistivity
R_P	radius of the powder distribution
s_{ij}	deviatoric stress in tensor form
S	source term in governing equation at liquid / vapor interface
t	time
t^*	fictitious time
T	temperature
T_m	melting temperature
T_{amb}	ambient temperature
\mathbf{u}	velocity in Cartesian vector form
v	velocity

v_n	interface velocity
V	volume
V_p	volume fraction of pearlite
$x_i n$	i -component node size
x	material constant
x_i	Cartesian coordinates ($x_1=X$, $x_2=Y$, and $x_3=Z$)
y	material constant

Subscripts

C	carbon
G	gas
i	integer (1, 2, or 3) index represents one of Cartesian direction
L	liquid
M	martensite
Ni	nickel
p	pearlite
P	powder
S	solid

ABSTRACT

A NUMERICAL AND EXPERIMENTAL STUDY FOR RESIDUAL STRESS EVOLUTION IN LOW ALLOY STEEL DURING LASER AIDED ADDITIVE MANUFACTURING PROCESS

by

Hyung Min Chae

Chairperson: Jyotirmoy Mazumder

One of the challenges in laser aided Direct Metal Deposition (DMD) process is control of the residual stress generated during the process due to thermal loads and solid state phase transformation. However, in situ residual stress monitoring in DMD process, used as an on-line sensor for a feedback control system, is difficult and also requires relatively high cost to accurately monitor mechanical deformations. Therefore, a fundamental understanding of the correlations between processing variables and the thermal and mechanical behaviors of material in DMD process is essential, because the residual stress field can be controlled in the stage of developing laser tool paths and the corresponding processing parameters. Mathematical models in DMD process are developed and utilized to obtain the correlations, rather than performing a series of experiments in the study. A self-consistent transient 3-D model is adopted to predict

thermal behaviors and the model is experimentally validated by comparing temperature history, melt pool flow, and deposition geometry with different processing parameters. The results from the thermal model are used to predict mechanical deformations in DMD process using a commercial software package ABAQUS with proper user subroutines. X-ray diffraction residual stress measurements are conducted for validation purpose, and the validated mathematical model is utilized to explain the evolution of stress in DMD process and to investigate the effects of processing parameters on the residual stress. The considered processing variables are metal powder flow rate, laser power, scanning speed, scanning direction, and deposition layer thickness. The residual stress is determined in three stages: thermal expansion by a heat source, restoration by melting, and thermal contraction by cooling, and the residual stress can be controlled by altering melt pool geometry with processing variables due to the dependence of residual stress on melt pool geometry. The most significant factor to determine the magnitude of the residual stress is the melt pool penetration to the substrate and the most influential parameter defining the residual stress profile along the depth direction is the amount of energy density.

CHAPTER I

INTRODUCTION

Laser aided Direct Metal Deposition (DMD) process, developed in the Center for Laser Aided Intelligent Manufacturing (CLAIM) at the University of Michigan, is an attractive and innovative laser aided manufacturing technique that produces a 3-D complex metallic shape pixel by pixel directly from CAD data (See Figure 1.1). Materials can be designed for a chosen performance using DMD process with a feedback control of deposition geometry and melt pool temperature with altered processing parameters. Mazumder and Qi [1] reviewed the state of the art of DMD. A selection of processing parameters, such as laser power, scanning velocity, scanning path, and powder flow rate, determines heat transfer and it plays a significant role in defining deposition geometry, and mechanical and metallurgical properties of the deposited material. Due to the characteristic of laser material processing of metallic product, mechanical deformations remains after the process due to severe thermal loads and solid state phase transformation, which may leads to premature failure during life cycle. Controlling heat transfer with providing optimized processing parameter set is, therefore, essential to achieve the required residual stress field of the DMD fabricated product. A fundamental understanding of the processing variable effects on the heat transfer and residual stress delivers an optimal parameter set for required criteria, and the set will be assigned in the

stage of generating laser tool paths. Since DMD process involves sequence of melting and solidification, mathematical simulations with different processing conditions, rather than a series of experiments, have been performed to understand physical phenomena in the laser material processing.

To date, tremendous efforts have been made to analytically and numerically study the effects of processing parameters on thermal behavior in laser additive manufacturing. Hoadley and Rappaz [2] investigated the relationship between laser power, scanning velocity, and deposition height using a 2-D finite element model, but they ignored fluid flow in the model. Melt pool shape was predicted by a simplified 3-D analytical heat transfer model [3], and the model was to guide processing engineers as choosing parameters. Kelly and Kampe [4] correlated cooling curves and phase transformation in multi-layer depositions with different scanning velocities using a simplified 2-D numerical model. The recent improvement of CPU performance has allowed numerically solving for more complex 3-D physical problems. A 3-D transient finite element model [5], using an energy balance equation, was developed to predict deposition geometry with different scanning speeds and powder flow rates. The model first predicted the melt pool, and governing equations are repeatedly solved with an addition of thin layer, but the model did not include the coupled heat transfer between temperature and fluid flow. Thermo-kinetic model [6] was developed to investigate the effects of substrate size and idle time between deposition layers on microstructure and hardness of the material. The authors used a 3-D finite element heat transfer model to predict temperature fields with assuming all powder particles reach liquidus temperature before falling into the laser melted pool, but convective term due to fluid motion inside melt pool was not considered

in the model. The alternate-direction explicit finite difference method model [7] was developed to numerically simulate thermal behaviors and to investigate how cooling cycles are controlled by different laser processing parameters, which determines microstructure and mechanical properties of the laser processed material. However, the authors also used a heat conduction model with ignoring fluid flow on a simplified cylindrical geometry and laser-powder interaction during powder travel below the nozzle is not included in the model.

In addition to thermal model in laser additive manufacturing processes, many authors [8-14] have conducted research to predict the residual stress using mechanical deformation models and to investigate the effects of processing variables on the stress field. Kahlen and Kar [8] developed a simplified 1-D heat transfer model to calculate temperature profile and to predict the residual stress using thermal strain only in their constitutive model. Deus and Mazumder [9] constructed a 2-D thermal model to predict temperature field with geometry dependent laser beam absorptivity and the mathematically calculated temperature history was used to predict the residual stress, but melt pool flow effects were ignored in the study. A thermal gradient map with non-dimensional process variables [10] was constructed by a 2-D conductive heat transfer model to quantify the effects of processing parameters and melt pool size on the residual stress. Dai and Shaw [11] built a 3-D finite element model to investigate how the residual stress develops with temperature change during laser material deposition, and the model was used to study the effects of processing parameters and material properties on the thermal and mechanical behaviors of the laser processed material. However, they did not consider the effects of changes in melt pool shape and deposition geometry on the

behaviors. Ghosh and Choi [12-14] developed a 3-D finite element model to predict temperature and the residual stress distributions for single- and multi- layer depositions. The model described the significant effect of solid state phase transformation on the residual stress field and it was used to investigate the correlation of deposition pattern to the stress field. The heat transfer model did not consider convection inside melt pool and the metal powder was added by pre-defined deposition geometry obtained from experimental data. Therefore, the effects of melt pool shape with different processing parameters on thermal and mechanical behaviors could not be investigated in the model.

In this study, a self-consistent transient 3-D model for depositing metal powders with laser as a heat source, which has been developed in the previous research [15, 16], has been used in thermal analyses of DMD process. Level-set method allows tracking the evolution of the liquid / vapor interface during the process; thus the effects of changes in deposition / melt pool geometry with processing variables on the residual stress field can be analyzed in this study. Non-equilibrium partitioning at the solidification front is adopted in solidification process due to the characteristic of laser aided manufacturing process. The deposition of AISI 4340 steel on a low carbon steel, AISI 1018 steel, is numerically simulated using two different types of lasers (CO₂ and DISC laser) with TEM₀₀, TEM₀₁*, and Top hat modes. Since AISI 4340 steel has a number of alloying elements as shown in Table 2.2, alloying elements of carbon and nickel are chosen to define the mushy zone and to examine the solute transport of the elements in liquid iron solution. The temperature histories from the model are utilized to predict metallurgical phases using empirical relationships because martensitic phase transformation occurs in laser processing of medium carbon steel and it significantly influences the mechanical

deformation in the process [17]. To validate the mathematical thermal model, temperature history, melt pool flow velocity, and the changes in geometry with processing conditions have been compared with experimental results and the numerical results agree with experimental measurements. The temporal evolution of geometry, temperature, and solid state phase transformation are imported into a commercial software package ABAQUS with proper user subroutines to predict the mechanical deformation of the DMD fabricated material and the model is experimentally validated by X-ray diffraction residual stress measurements. The model explains the evolution of residual stress with heating / melting / solidification / cooling and the dependence of the residual stress on melt pool geometry; therefore, the melt pool geometry effects with altered processing conditions are necessary to be included in the stress analysis in DMD process. Then, martensitic phase transformation effects also have been investigated in the study, and processing parameters such as laser power, laser scanning speed, powder flow rate, scanning direction, and deposition layer thickness have been varied to investigate how the parameters influence the residual stress distribution / magnitude.

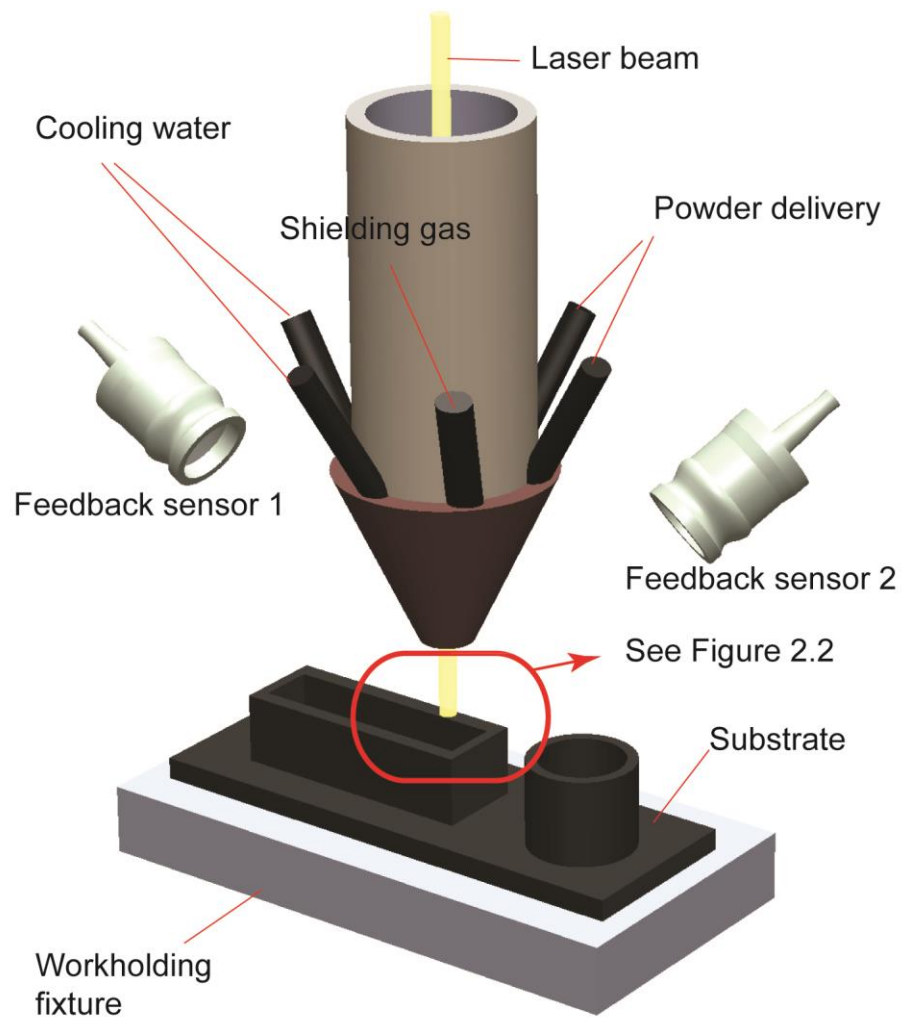


Figure 1.1 Direct Metal Deposition (DMD) process with feedback sensors

CHAPTER II

NUMERICAL MODELING: THERMAL MODEL

2.1 Introduction

In Direct Metal Deposition (DMD) process, powdered metal particles interact with laser beam during the travel from powder nozzle to substrate. Laser energy is attenuated by the powder particles and the particles are heated and melted by the absorbed laser energy. The attenuated beam energy and the energy carried by metal particles are mostly dissipated into the substrate by conduction once deposited, and the rest of energy is lost by radiation and convection to the ambient. It should be noted that the energy loss by evaporation is ignored in the study since DMD process typically uses relatively lesser laser intensity (an order of 10^5 W/cm²) than other laser aided manufacturing processes.

A self-consistent transient 3-D model was developed for laser material interaction in laser aided welding / drilling processes in the Center for Laser Aided Intelligent Manufacturing (CLAIM) at the University of Michigan. For numerical analyses in laser additive manufacturing process, the model has been modified with considering powder addition which includes laser powder interaction during powder delivery. To develop a mechanical deformation model in DMD process, an accurate temporal evolution of

temperature, geometry, and metallurgical phases should be obtained from the thermal model with minimal computational costs; therefore, non-equilibrium partitioning is considered in solidification process, which influences solute transport and cooling behavior in DMD process, ternary system (carbon-nickel-iron) is analyzed with two binary sub-systems for AISI 4340 steel deposition, metallurgical phases such as martensite and pearlite are predicted with empirical relationships, and two dimensional the Courant-Friedrichs-Lewy condition has been used to optimize the time step and mesh size. The modified thermal model accurately predicts temperature, melt pool flow, solute transport, deposition geometry, and solid state phase transformation in DMD process and it is experimentally validated by comparing temperature history, fluid flow, and the deposition geometry with processing variables. Temperature of the material in the process is monitored by an infrared pyrometer and the linear velocity of the melt pool surface is obtained from successive melt pool images taken by a high speed CCD camera.

2.2 Assumptions

The assumptions made in the thermal model in DMD process are provided below

- 1) Material properties at the liquid / solid interface are determined by the law of mixture
- 2) Material properties at the liquid / vapor interface are smoothed by a sinusoidal function (See Equation 2.2) to increase the degree of continuity across the interface
- 3) Thermo-physical material properties at high temperature are extrapolated
- 4) Fluid flow is laminar and incompressible

- 5) Plasma is not considered for simplicity
- 6) Laser attenuation due to powder particles follows the Beer-Lambert law but the dynamic motion of the particles into the melt pool is ignored
- 7) Effects of shielding gas on flow motion / heat transfer are ignored
- 8) Evaporation of the material is negligible in DMD process
- 9) Liquid / vapor interface moves with powder addition and advection force of the laser melted pool
- 10) Mass diffusion in solid state is ignored
- 11) There is no diffusion phase transformation within the martensite phase transformation temperature

2.3 Boundary conditions / Governing equation / Flow chart

In the present analyses, AISI 4340 steel powder is deposited on a substrate of AISI 1018 steel, and the simulation domain is $27 \times 14 \times 5$ mm in x_i direction where the subscript i is the integer (1, 2, or 3) index that represents one of Cartesian direction. The simulation model of plane symmetric ($x_2=Y=0$) uses non-uniform meshes to reduce computational cost as shown in Figure 2.1. The elemental composition [18] and thermo-physical properties of AISI 4340 steel used in the thermal analyses are provided in Table 2.2 and 2.3, respectively. The thermo-physical material properties at high temperature are extrapolated due to the limitation of an access in database and the material properties, such as density, thermal conductivity, specific heat, enthalpy, solute concentration, and mass diffusion coefficient at mushy zone (the liquid / solid interface) are determined by the generalized law of mixtures as follow [19-23]

$$pr = f_L \cdot pr_L + f_S \cdot pr_S \quad \text{Equation 2.1}$$

where pr is the material property, f is the volume fraction of the phase, and the subscript L and S represent the liquid and solid phase, respectively.

The material properties at the liquid / vapor interface rapidly changes compared to those at the liquid / solid interface. To guarantee full convergence with significant difference in material properties, a sinusoidal function $H(\varphi)$ is used to smooth out the difference across the interface as follows (also See Figure 2.3)

$$H(\varphi) = \begin{cases} 1 & \text{if } \varphi < -\varepsilon \\ 1 - 0.5 \left(1 + \frac{\varphi}{\varepsilon} + \left(\frac{1}{\pi} \right) \sin \left(\frac{\pi \varphi}{\varepsilon} \right) \right) & \text{if } |\varphi| \leq \varepsilon \\ 0 & \text{if } \varphi > \varepsilon \end{cases} \quad \text{Equation 2.2}$$

where φ represents the state of matter such that positive and negative φ values represent gas and liquid (or solid) phases, respectively, and ε is the smoothing thickness. The smoothing thickness chosen in this study is $2x_{3n}$ (x_{3n} : mesh size in x_3 direction), and the material properties at the liquid / gas interface are calculated by

$$pr(\varphi) = pr_L + (pr_L - pr_G) \cdot H(\varphi) \quad \text{Equation 2.3}$$

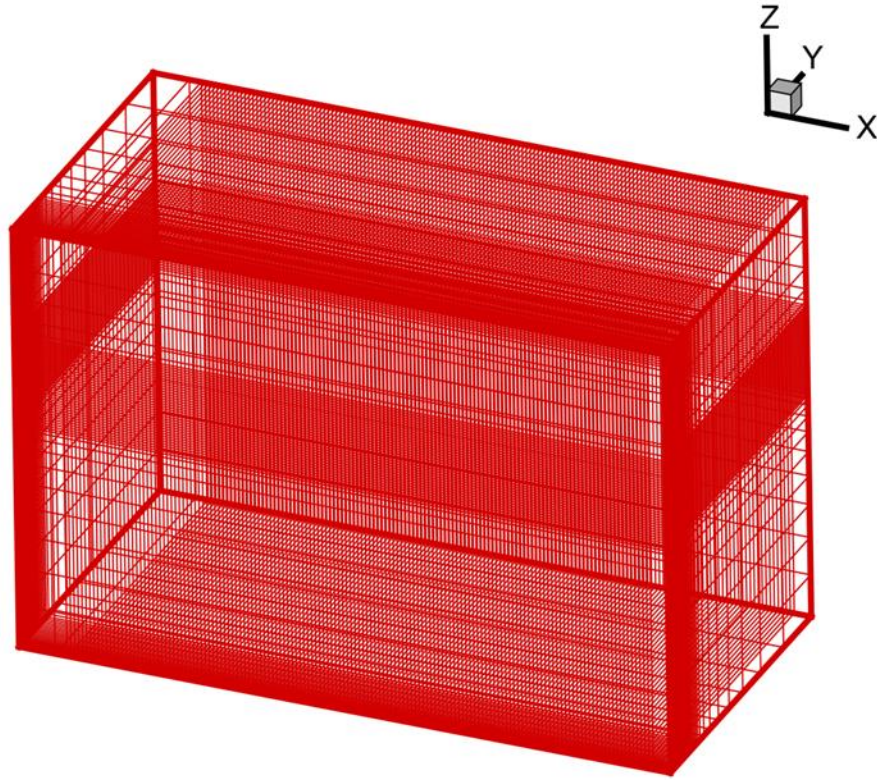


Figure 2.1 Numerical simulation domain: plane symmetric ($Y=0$) with non-uniform mesh for minimal computational cost

Table 2.1 Temperature dependent electrical resistivity of AISI 4340 steel

Electrical resistivity (ohm-cm)	Temperature (K)
2.48E-5	293.15
2.98E-5	373.15
5.52E-5	673.15
7.97E-5	873.15

Table 2.2 Elemental composition of AISI 4340 steel [18]

Element	<i>wt %</i>
C	0.43
Mn	0.7
P	0.008
S	0.008 (Max)
Si	0.23
Cr	0.81
Ni	1.75
Cu	0.16
Al	0.90-1.35
Ti	0.01
N	0.01 (Max)
O	0.0025 (Max)
Co	0.01
Mo	0.25

Table 2.3 Material properties of AISI 4340 steel used in thermal analyses

Property	Symbol	Value	Unit
Melting temperature	T_m	1800.4	K
Latent heat of fusion	L_m	2.26E+5	J/kg
Solid density	ρ_s	7870	Kg/m^3
Liquid density	ρ_L	6518.53	Kg/m^3
Solid thermal conductivity	k_s	See Figure 2.2 (a)	$W/m K$
Liquid thermal conductivity	k_L	43.99	$W/m K$
Solid specific heat	C_{ps}	See Figure 2.2 (b)	$J/kg K$
Liquid specific heat	C_{pL}	804.03	$J/kg K$
Kinetic viscosity	μ	4.936E-7	m^2/sec
Laser absorptivity for flat surface	η	See Equation 2.7 and Figure 2.5	
Carbon content	C_C	See Table 2.2	$wt\%$
Nickel content	C_{Ni}	See Table 2.2	$wt\%$
Electrical Resistivity	R_E	See Table 2.1	$ohm-cm$
Equilibrium partition coefficient for carbon	$k_{e,C}$	0.2	
Equilibrium partition coefficient for nickel	$k_{e,Ni}$	0.9	

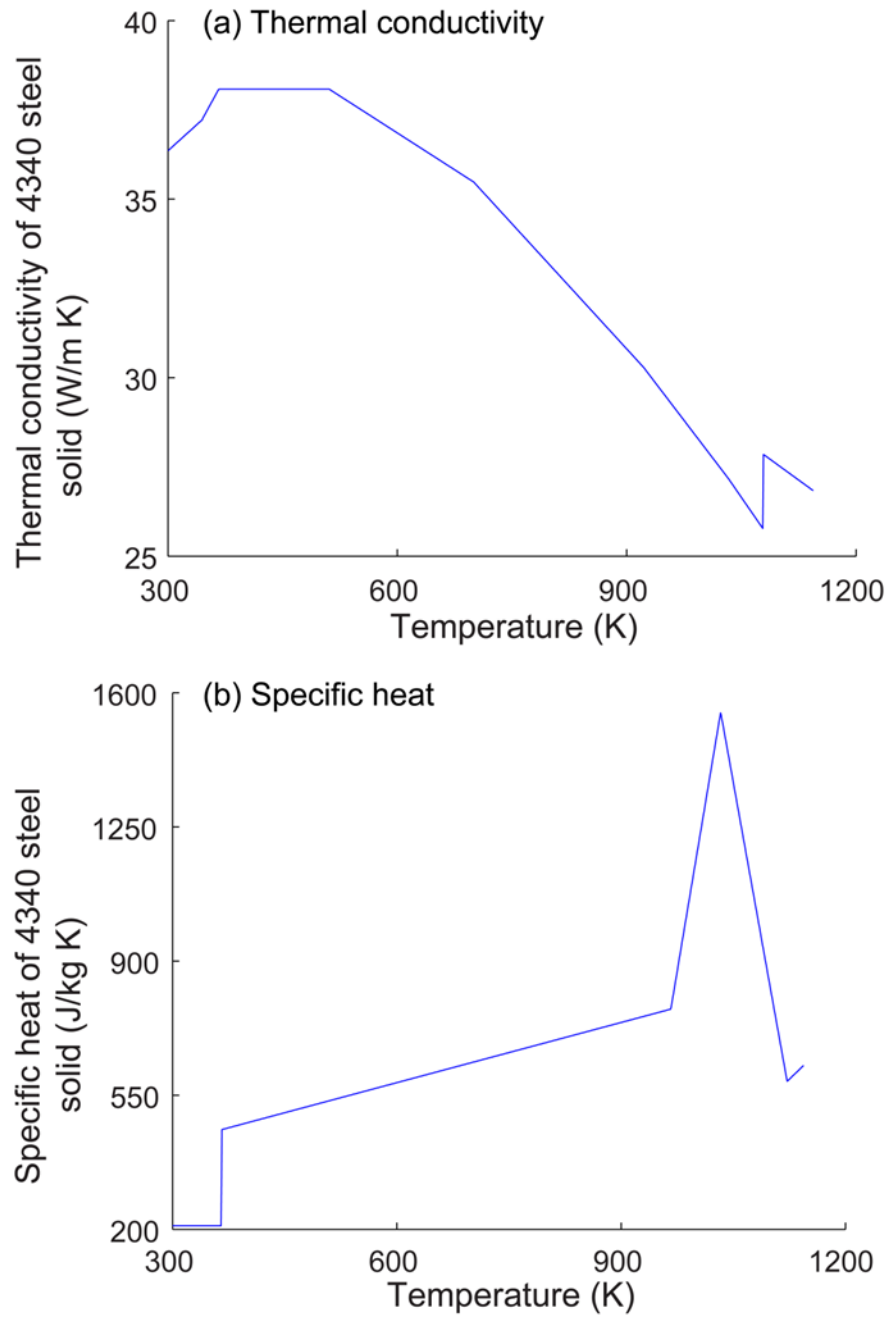


Figure 2.2 Thermo-physical material properties of AISI 4340 steel: (a) Thermal conductivity (b) Specific heat [24]

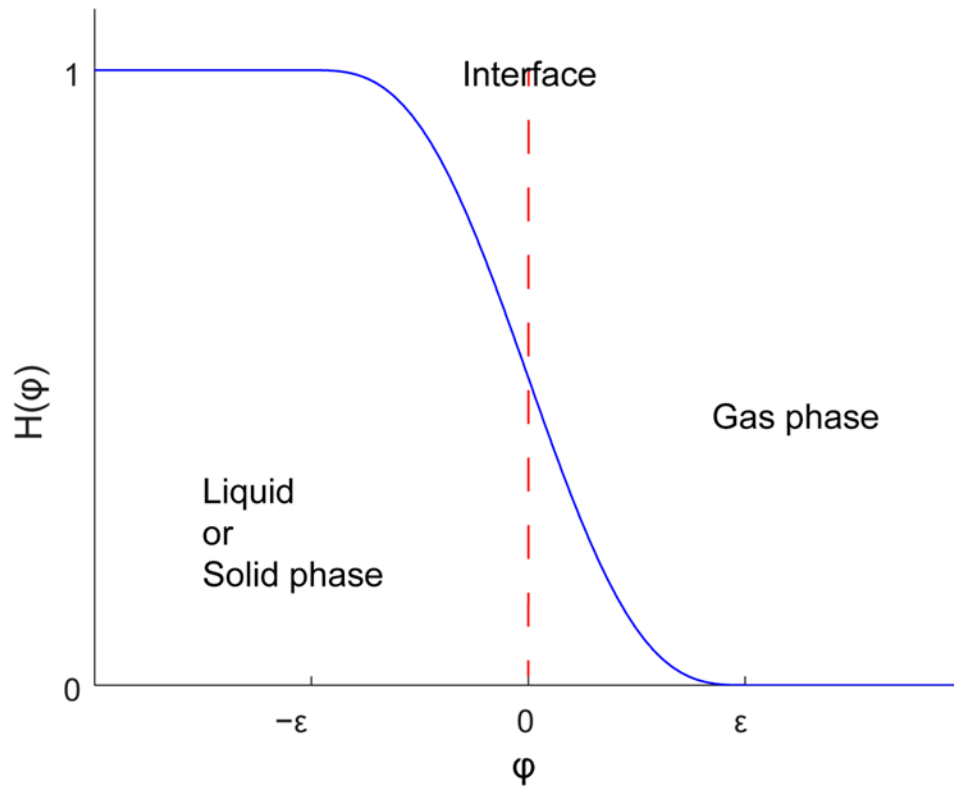


Figure 2.3 A sinusoidal function, used to smooth out the significant difference in material properties across the liquid / gas interface, guarantees the full convergence during computation

AISI 4340 steel is composed of a number of alloying elements as provided in Table 2.2. Two significant alloying elements, carbon and nickel, among the elements of AISI 4340 steel are chosen in thermal analyses for simplicity. Carbon is the significant alloying element in steel, and nickel is the primary alloying element in AISI 4340 steel and it remains in iron-carbon solution without forming carbide compounds. Since the DMD fabricated product is rapidly heated, melted, solidified, and cooled by a cooling rate above -650 K/s from austenite temperature, diffusions in solid state material during the process is assumed to be negligible. The mass transport of carbon and nickel elements

in liquid iron solution can be predicted by Equation 2.13 if a ternary phase diagram with proper diffusion coefficients is provided, which accurately provides solute transport of the carbon-nickel-iron ternary system and the mushy zone information such as solid / liquid volume fraction of each element. However, the numerical model uses two different solute diffusion equations for carbon and nickel in liquid iron solution (two of binary subsystems) due to the limit of access in database of the ternary system. Once material cools down and the temperature is within liquidus and solidus temperature, solid C_S and liquid C_L compositions are obtained from dynamic non-equilibrium binary phase diagrams, described in Section 2.4. Liquid volume fraction at mushy zone is then calculated by lever rule (see Equation 2.4). It should be noted that the sum of liquid and solid volume fraction must be unity for mass conservation.

$$f_{total,L} = f_C + f_{Ni} = \frac{C_C - C_{C,S}}{C_{C,L} - C_{C,S}} + \frac{C_{Ni} - C_{Ni,S}}{C_{Ni,L} - C_{Ni,S}} \quad \text{Equation 2.4}$$

where C is the solute concentration and the subscript C and Ni represent carbon and nickel, respectively. To solve for the solute concentration in the diffusion equations, temperature dependent diffusion coefficients D in iron-solution for carbon and nickel [25] are used as in Equation 2.5 and 2.6, respectively.

$$D(cm^2 / s) = 0.0012 \cdot (\text{Carbon wt \%}) \exp(-13.8/RT) \quad \text{Equation 2.5}$$

$$D(cm^2 / s) = 4.92 \cdot 10^{-3} \exp(-16.2(kcal / mol) / RT) \quad \text{Equation 2.6}$$

The amount of carbon and nickel contents of AISI 4340 steel powder are given at the laser melted surface and the carbon content of AISI 1018 steel is given at the melting

front of the substrate as seen in Figure 2.4, which describes the overall boundary conditions in the DMD thermal model such as energy balance and solute transport. It should be noted that evaporation of the material during the process is ignored.

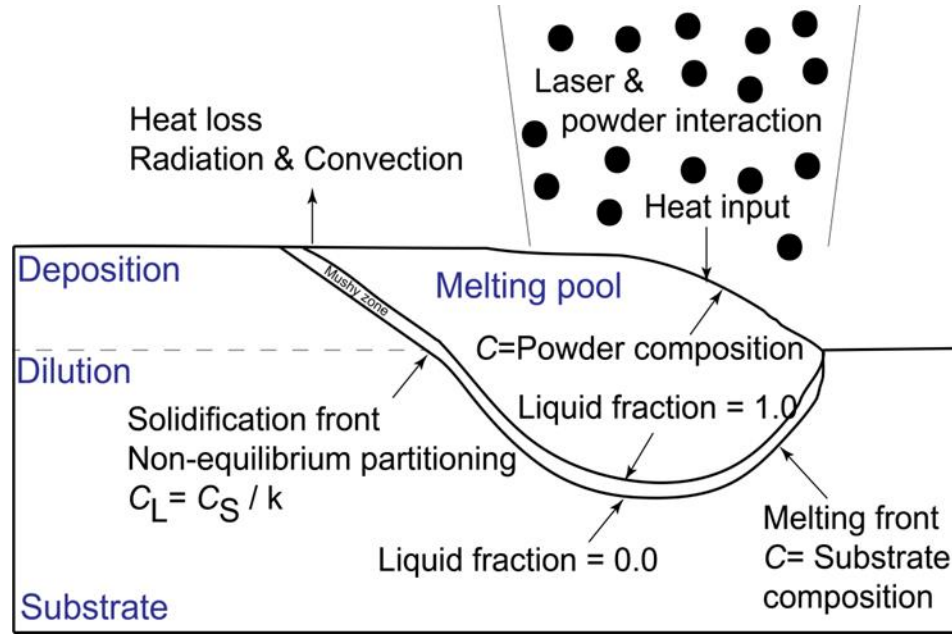


Figure 2.4 Boundary conditions used in the DMD thermal model

Several types of high power lasers are commonly utilized in real DMD production line. In this study, DISC and CO₂ lasers are selected to conduct the mathematical simulations and experiments. Top hat-CW-DISC laser has a wavelength of 1050 nm and 300 micron focused beam, TEM₀₀-CW-CO₂ laser has a wavelength of 10.6 micron and 500 micron focused beam, and TEM₀₁*-CW-CO₂ laser has a wavelength of 10.6 micron and 1 / 2 / 4 mm focused beams. Since laser energy is the main heat source in DMD process and laser absorption of the material depends on wavelength and temperature, the

temperature / wavelength dependent absorption coefficient for CO2 laser, proposed by Bramson [26], is obtained as

$$\eta(T) = 0.365 \sqrt{\frac{R_E(T)}{\lambda}} - 0.0667 \frac{R_E(T)}{\lambda} + 0.006 \left(\frac{R_E(T)}{\lambda} \right)^{3/2} \quad \text{Equation 2.7}$$

where η is the absorption coefficient, R_E is the electrical resistivity of the material, and λ is the laser wavelength. For DISC laser, temperature dependent absorption coefficient [27] is used in the model as seen in Figure 2.5.

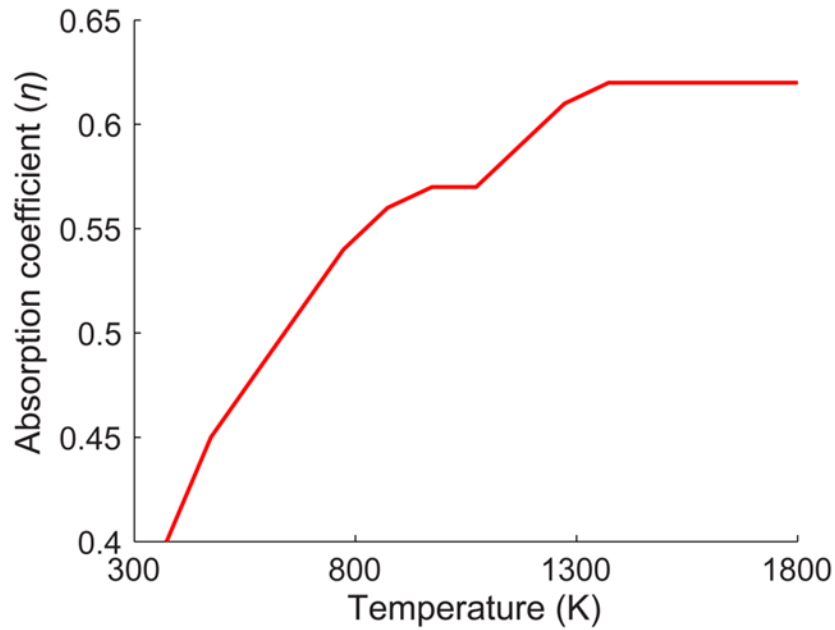


Figure 2.5 Temperature dependent absorption coefficient of AISI 4340 steel with DISC laser

As laser beam is delivered from DMD nozzle to a substrate, there is an efficiency loss by radiation absorption in metallic particles [28], angles of incident, and surface

roughness of the substrate. For simplicity, the effects of radiation absorption in the particles and substrate surface roughness on laser efficiency are ignored in this study. However, the changes in absorption due to an incident angle between material surface and laser beam is continuously adjusted with material deposition. The absorptance of powdered metal is greater than that of a dense material due to pores and multiple reflections between particles [29], thus 0.4 is chosen as the absorption coefficient of AISI 4340 steel powder with CO2 laser. Due to the limit of database in DISC laser case, the same absorption coefficient of bulk material with DISC laser for the metallic powder absorption coefficient is used when DISC laser is a heat source.

To consider energy balance in DMD process, the authors [15, 16, 30] developed the laser-powder interaction model using the Beer Lambert Law as

$$q'(r,l) = q(r) \exp(-A_P N l) \quad \text{Equation 2.8}$$

where $q'(r,l)$ is the attenuated beam intensity, $q(r)$ is the beam intensity, A_P is the powder particle area exposed to the beam, N is the number of powder particles in a unit volume V , and l is the powder travel distance. With an assumption that powder particles are distributed in Gaussian form, the radial distribution $N(r)$ is calculated as

$$N(r) = \frac{Flow_P}{v_P \rho_P (\pi R_P^2) V} \exp\left(-2 \frac{r^2}{R_P^2}\right) \quad \text{Equation 2.9}$$

where $Flow_P$ is the powder flow rate, R_P is the radius of the powder distribution, v_P is the powder travel velocity, and ρ_P is the powder density. The axial distance l is divided into several steps along the Z axis to calculate the beam attenuation using Equation 2.8, and

the temperature and the state of powder material at the laser melted surface are determined by Equation 2.10.

$$E_P = \begin{cases} m_P (Cp_L(T_P - T_m) + L_m + Cp_S(T_m - T_{amb})) & \text{if } T_P > T_m \\ m_P (Cp_S(T_m - T_{amb}) + L_m f_L - L_m f_S) & \text{if } T_P = T_m \\ m_P (Cp_S(T_P - T_{amb}) - Cp_S(T_m - T_P) - L_m) & \text{if } T_P < T_m \end{cases} \quad \text{Equation 2.10}$$

where E_P is the energy absorbed by powder particles, m is the mass, Cp is the heat capacity, T_m is the melting temperature of metallic powder, T_{amb} is the ambient temperature, L_m is the heat of fusion, and the subscript P represents the metallic powder.

With provided boundary conditions, temperature, fluid flow, and species are solved by Equation 2.11, 12, and 13 in a coupled manner using SIMPLE algorithm, and the overall flow chart of the thermal simulation is shown in Figure 2.6. The equations are solved for velocity components and scalar variables such as temperature, solute concentration, pressure, and material properties; therefore, the equations are discretized by an upwind-differencing scheme.

$$\frac{\partial(\rho h)}{\partial t} + \nabla \cdot (\rho \mathbf{u} h) = \nabla \cdot (k \nabla T) - \nabla \cdot [\rho (h_l - h) \mathbf{u}] + S_{energy} \quad \text{Equation 2.11}$$

$$\frac{\partial(\rho u_i)}{\partial t} + \nabla \cdot (\rho \mathbf{u} u_i) = \nabla \cdot \left(\mu_L \frac{\rho}{\rho_L} \nabla u_i \right) - \frac{\mu_L}{K} \frac{\rho}{\rho_L} u_i - \frac{\partial p}{\partial x_i} + S_{velocity} \quad \text{Equation 2.12}$$

$$\begin{aligned} \frac{\partial(\rho C_L)}{\partial t} + \nabla \cdot (\rho \mathbf{u} C_L) &= \nabla \cdot (\rho D_L \nabla C_L) + \\ &\frac{\partial(\rho f_s C_L)}{\partial t} - k_{ne} C_L \frac{\partial(\rho f_s)}{\partial t} + \nabla \cdot [\rho D_L \nabla (f_s (k_{ne} - 1) C_L)] + S_{solute} \end{aligned} \quad \text{Equation 2.13}$$

where, h is the enthalpy, t is the time, \mathbf{u} is the velocity in Cartesian vector form ($\mathbf{u} = u_1\mathbf{i} + u_2\mathbf{j} + u_3\mathbf{k}$), k is the thermal conductivity, μ is the viscosity, K is the isotropic permeability, p is the pressure, $D_L (= f_L \cdot D_L)$ is the liquid diffusion coefficient in iron solution, k_{ne} is the non-equilibrium partitioning coefficient, and S is the source term in each equation shown in Table 2.4.

Table 2.4 Source term at the liquid / vapor interface in each governing equation

Governing equation	S	Description
Temperature	$q' - \varepsilon_m \sigma (T - T_m)^4 - C_{conv} (T - T_m)$	Attenuated beam energy Radiation loss Convection loss
x_i -momentum	$-e_i \left(\sigma_T \mathbf{n} \mathbf{K} - \nabla_s T \frac{d\sigma_T}{dT} \right)$	Capillary force Thermo-capillary force
Species	$C_C + C_{Ni}$	Powder addition

The Courant-Friedrichs-Lewy condition (CFL condition) is necessary to limit the mesh size $\Delta x_i n$ and time interval Δt for convergence due to the hyperbolic PDEs. Since heat, Navier-Stokes, and solute diffusion equations are the second order system, CFL condition has the following form of

$$\Delta t \leq c \cdot \frac{(\Delta x_i n)^2}{v} \quad \text{Equation 2.14}$$

where c is the constant and v is the maximum velocity of the melt pool.

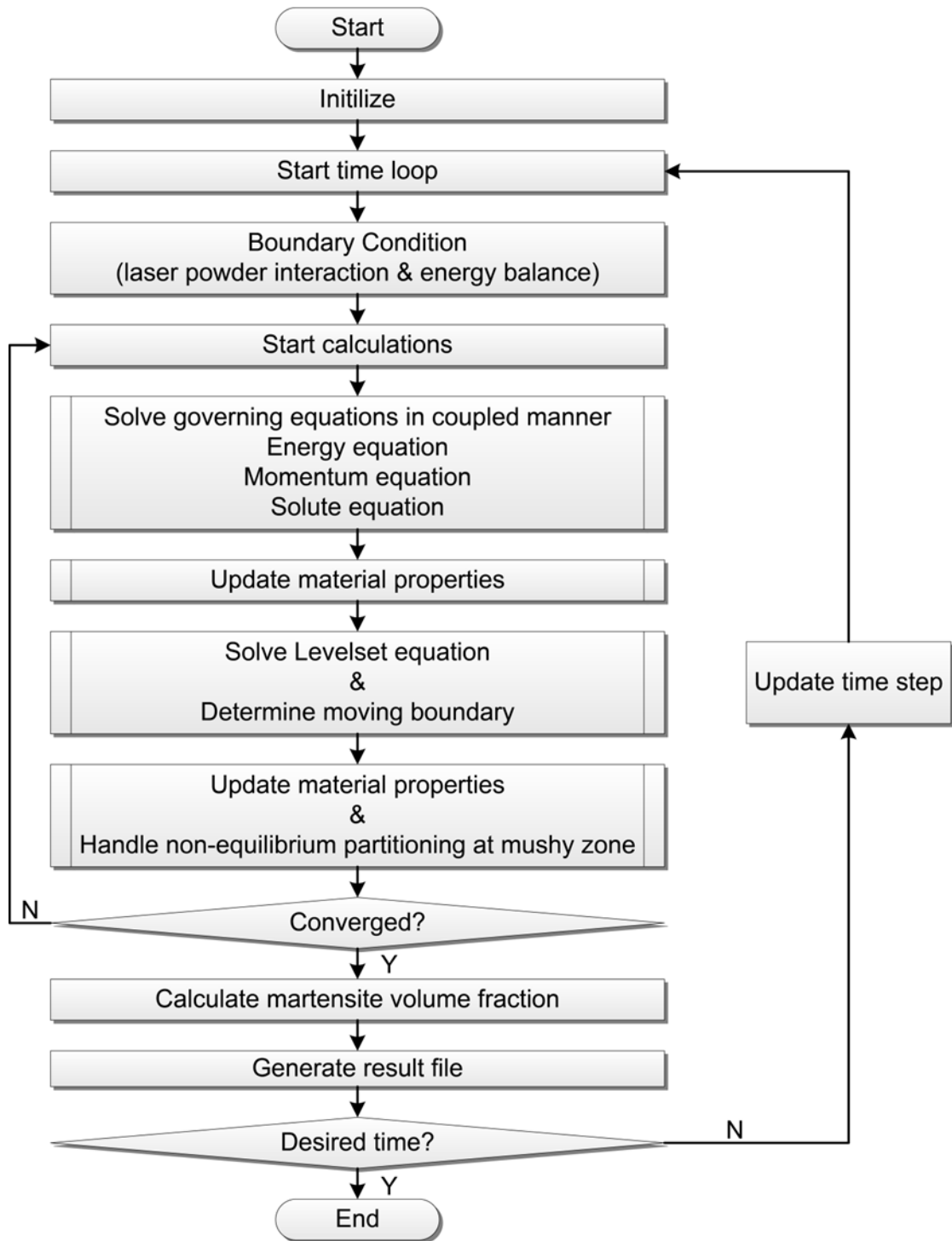


Figure 2.6 Flow chart of thermal model in DMD process

The liquid / vapor interface changes with metallic powder deposition during DMD process and the evolution of the interface is tracked by level-set method, which was developed by Osher and Sethian [31]. The interface Φ is defined in a 3-D Cartesian coordinate system by the zero level-set function such that $\Phi = \{(x, y, z) | \varphi(x, y, z) = 0\}$. The detailed explanation of level-set method in laser material processing can be found in the previous numerical studies in laser welding / drilling process [32]. The liquid / vapor interface moves normal to the interface with a speed F , and the speed function F is decomposed into the powder force F_P , the advection force F_{adv} , and the force due to the liquid / vapor interface curvature F_{curv} as

$$F = F_P + F_{adv} + F_{curv} \quad \text{Equation 2.15}$$

where F_P is $m_P(r)v_P / \rho_P$ and F_{adv} is $\mathbf{u}(x_i, t)$. The curvature force F_{curv} is ignored for simplicity in this study, and the auxiliary function φ in the level-set equation is defined as

$$\frac{\partial \varphi}{\partial t} = F |\nabla \varphi| = (F_{powder} + F_{adv}) |\nabla \varphi| \quad \text{Equation 2.16}$$

The auxiliary function φ is discretized by a second order space convex scheme to solve for φ . To reduce the computational time, only in a narrow band of interest is calculated as shown in Figure 2.7.

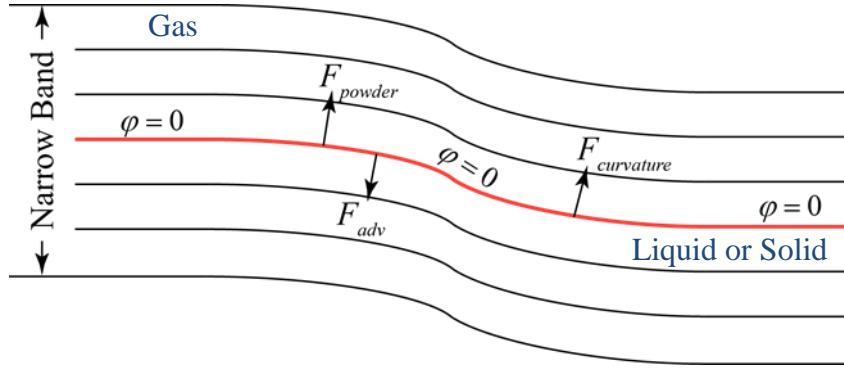


Figure 2.7 Schematic drawing of narrow band level-set method

2.4 Non-equilibrium partitioning in solidification

The alloy solute is rejected from an advancing solidification front into liquid zone because it is more soluble in the liquid alloy, and the ratio of the solid to the liquid composition is solute partitioning coefficient. Due to the characteristic of laser manufacturing process, rapid solidification, the partitioning of liquid and solid composition during solidification is non-equilibrium. Non-equilibrium partitioning coefficient [33] is thus adapted in the mathematical calculations as expressed in

$$k_{ne} = \frac{C_s}{C_{Li}} + \frac{k_e + \beta}{1 + \beta} \left(1 - \frac{C_L}{C_{Li}} \right) \quad \text{Equation 2.17}$$

where C_{Li} is the liquid solute concentration at the liquid-solid interface (See Figure 2.8), k_e is the equilibrium partitioning coefficient, and β is the dimensionless solidification rate defined as

$$\beta = a^2 |\mathbf{v}_n| / \left[(a + b) D_{ABs} \right] \quad \text{Equation 2.18}$$

where a and b are the mushy zone dimension, D_{ABs} is the inter-diffusion coefficient of species A with respect to species B in the solid phase, and v_n is the interface velocity. When the material temperature drops from melting temperature to liquidus temperature, the calculated solute concentration by Equation 2.13 at the temperature is recorded as an initial concentration C_{Lo} to calculate the composition of solid (C_S) and liquid (C_L) at the mushy zone with the following Equations 2.19 and 2.20.

$$C_S = C_{Lo} + e^{-\beta} (C_S^* - C_{Lo}) \quad \text{Equation 2.19}$$

$$C_L = C_{Lo} + e^{-\beta} (C_L^* - C_{Lo}) \quad \text{Equation 2.20}$$

where C_S^* and C_L^* are the solidus and liquidus composition obtained from the equilibrium phase diagram. From the calculated solidus and liquidus composition, dynamic non-equilibrium phase diagram can be built and Figure 2.9 shows an example of carbon-iron binary dynamic phase diagram. With considering non-equilibrium partitioning, solidus composition shifts to the left and the shift becomes greater as temperature decreases. However, liquidus composition is almost the same as the equilibrium liquidus composition.

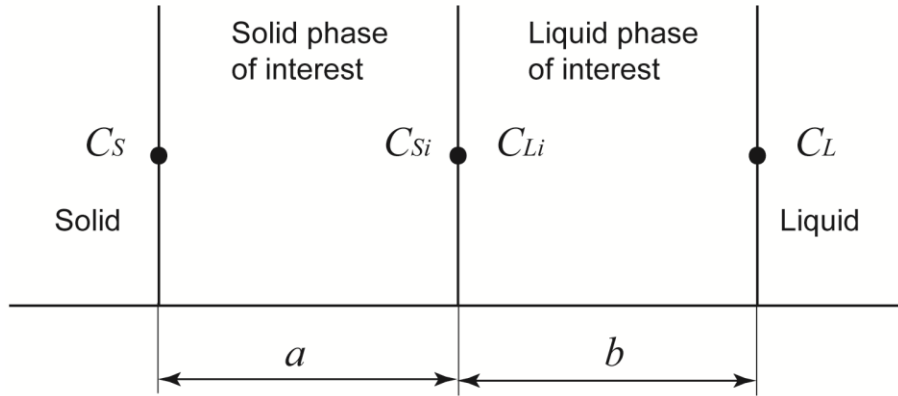


Figure 2.8 Geometric model for solid / liquid interface at mushy zone during solidification in laser material processing [33]

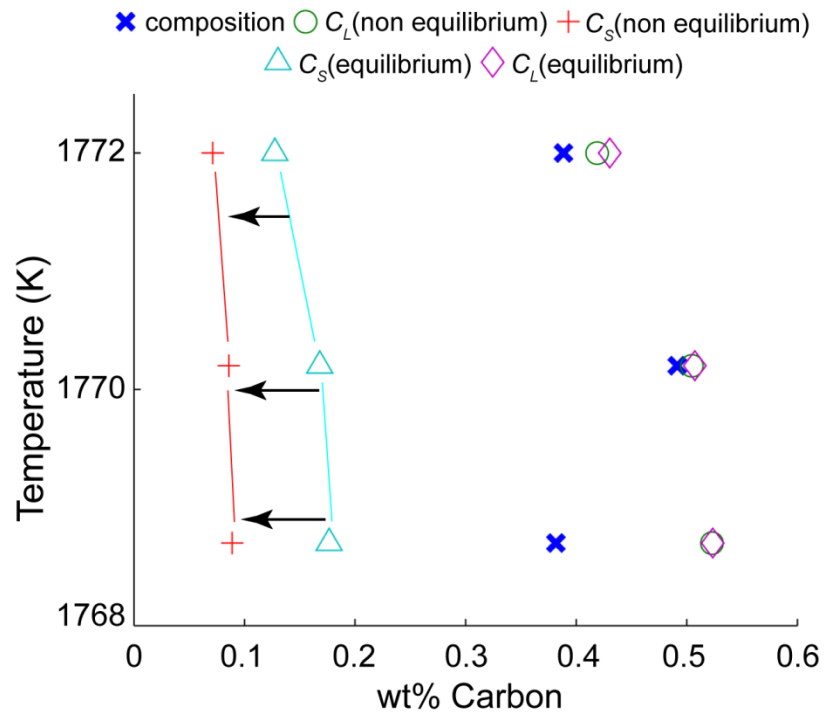


Figure 2.9 Dynamic non-equilibrium phase diagram of binary carbon-iron system

2.5 Numerical results

This section shows the numerical results from the mathematical model described in the previous sections. Temperature profile of AISI 4340 steel powder with various laser modes and the number of powder density along the Z axis are presented, and the optimal laser mode and powder distribution for better metallurgical properties of the DMD product is proposed. Temperature profile and fluid flow of the melt pool are also predicted and the temperature histories at different locations are used to calculate cooling rates. Lastly, solute transport of carbon and nickel in liquid iron solution is investigated with the Pectlet numbers.

2.5.1 Laser powder interaction

Powdered AISI 4340 steel temperature with three different CO2 laser beam modes, TEM_{00} , TEM_{01}^* , and Top hat mode, with the same power of 1400 Watts are calculated as shown in Figure 2.11, 2.12 (a) and 2.13, respectively. The normalized beam intensity profiles with different mode are compared in Figure 2.10 and the figure shows that the beam intensity of TEM_{00} mode is the greatest and the energy intensity of Top hat mode is the smallest, but evenly distributed. The maximum temperature is found where the peak intensity of the beam is located for TEM_{00} and TEM_{01}^* cases; however, the maximum temperature of the powder with Top hat mode is found at the edge of the beam. The number density of AISI 4340 steel powder is the greatest at the center of the beam with Gaussian distribution (See Figure 2.12 (b)) and the energy is uniformly distributed within the beam; therefore, the powders at the edge of the beam have the greatest energy absorption during travel, but the temperature difference between the edge and the center

of the beam is only 50 degrees (maximum temperature of 1150 Kelvin). Note that none of liquid state powder is found within the given processing parameter ranges in the study. With different powder flow rate and laser power, some of liquid powder particles can be observed.

The peak temperature of the powdered metal with TEM₀₁* mode is the highest even though the peak energy intensity of TEM₀₀ mode is the greatest among the three modes due to the difference in the amount of powders interacting with the laser energy during travel. In order to control the metallurgical properties, such as the size and the growth direction of grains, melt pool temperature control is essential. Therefore, using Top hat mode laser with proper laser power in DMD process is beneficial among the three different modes although the peak temperature with Top hat mode is the least.

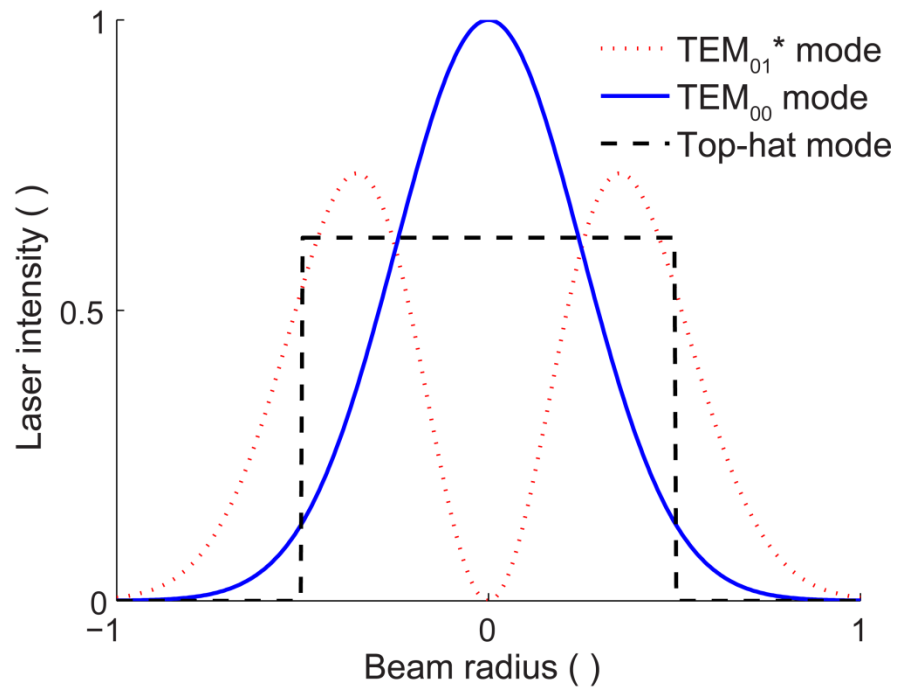


Figure 2.10 Laser intensity profile with various laser mode, TEM_{00} , TEM_{01}^* , and Top hat mode

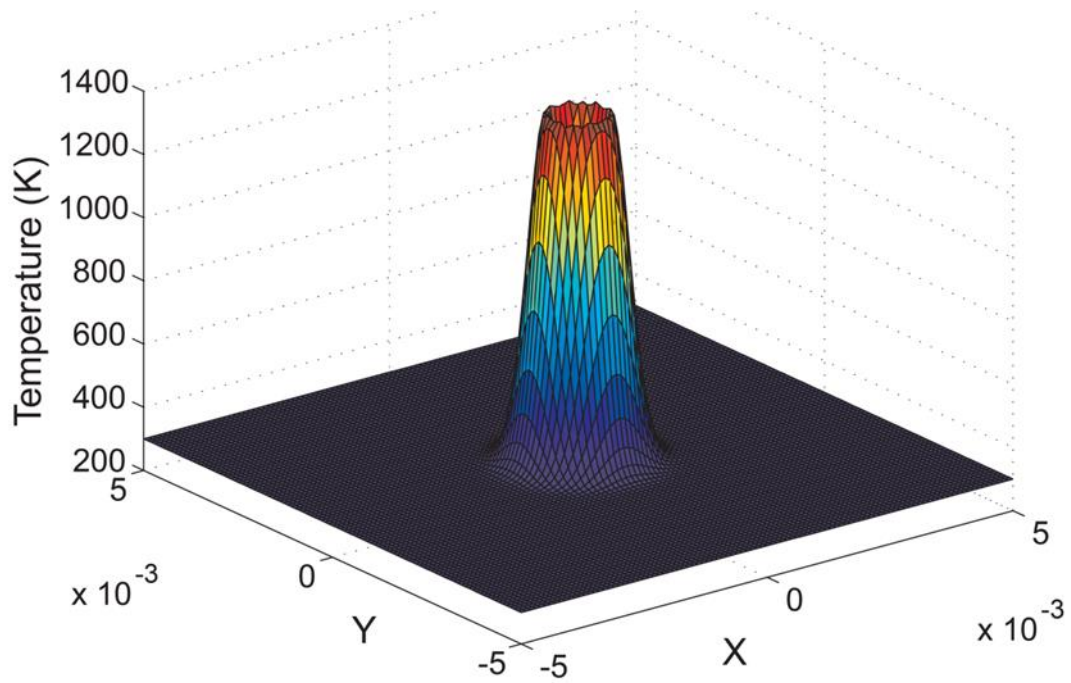


Figure 2.11 Powder temperature profile at the substrate with TEM_{01}^* -CO2 laser

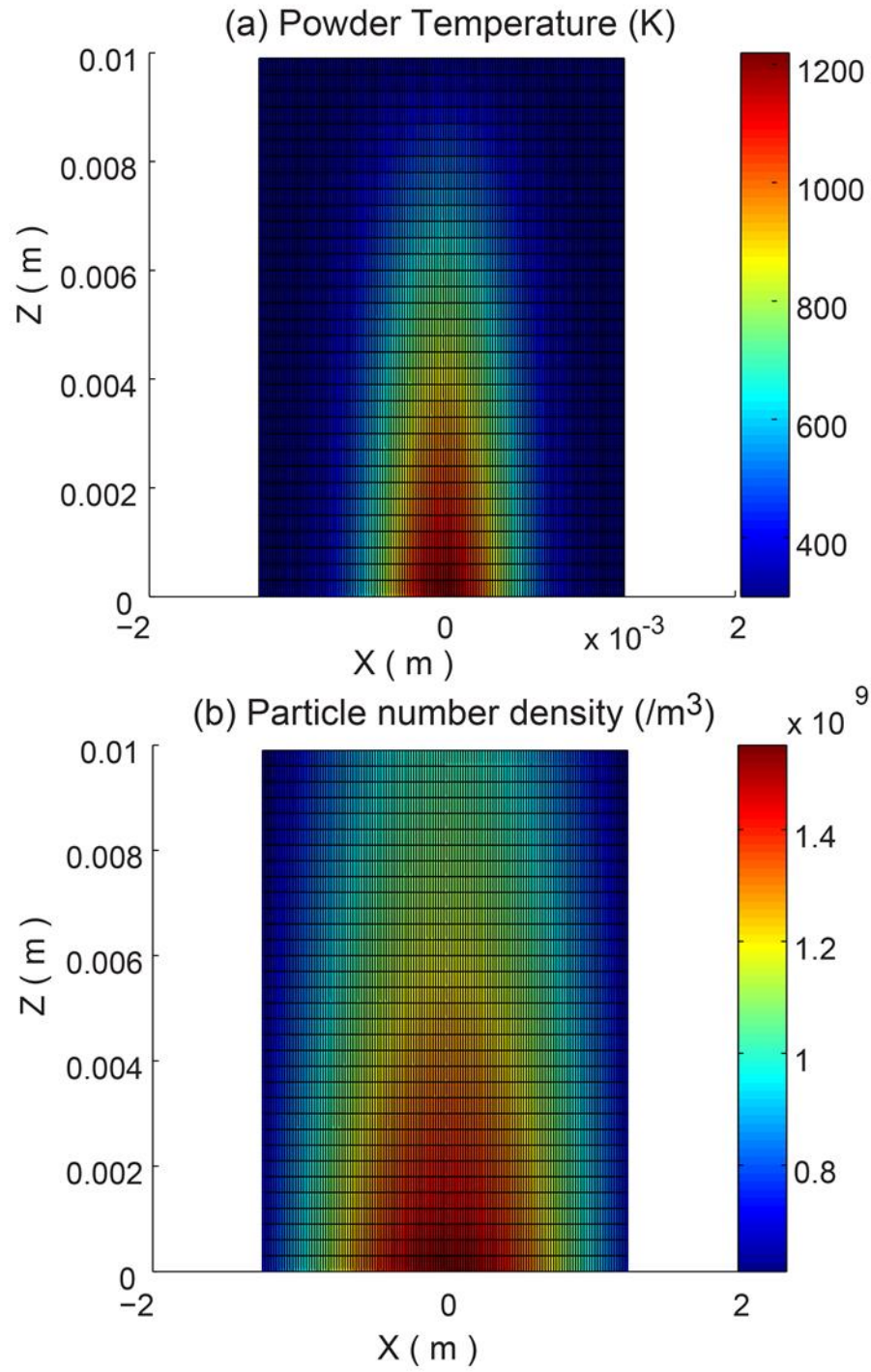


Figure 2.12 (a) Powder temperature (b) the number of powdered particles along the Z axis with TEM₀₀-CO₂ laser

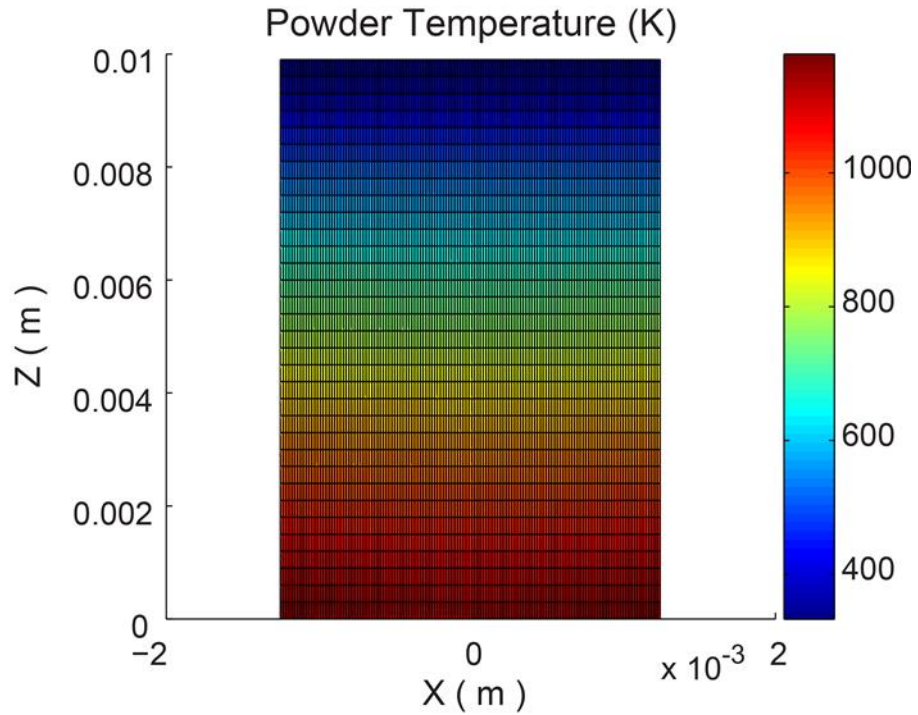


Figure 2.13 Powder temperature along the Z axis Top hat-CO2 laser

2.5.2 Temperature / fluid flow / solute transport

Two different lasers (DISC and CO2 lasers) are used in this section to predict the evolution of temperature, fluid flow, and solute transport. Figure 2.14 shows the results with a 1 mm Top hat-CW-DISC laser beam. The processing parameters used in the model are laser power of 1350 Watts, scanning speed of 21.2 mm/s, and AISI 4340 steel powder flow rate of 3.6 g/min. The maximum temperature of the melt pool and the rising time to melting temperature found in the simulation are 2200 Kelvin and 0.19 seconds, respectively. The area chosen for measuring the rising time is the top surface of the substrate because the material above the substrate was in gas state before the material deposition.

Figure 2.15 shows the temperature field with a 2 mm TEM₀₁*-CW-CO2 laser of 2000 Watts, scanning velocity of 10 mm/s, and the powder flow rate of 14 g/min. The maximum temperature of the melt pool and the rising time to melting temperature found in the model are 2020 Kelvin and 0.16 seconds, respectively. The temperature contour in the figure shows that the temperature gradient is the greatest right below the melt pool interface.

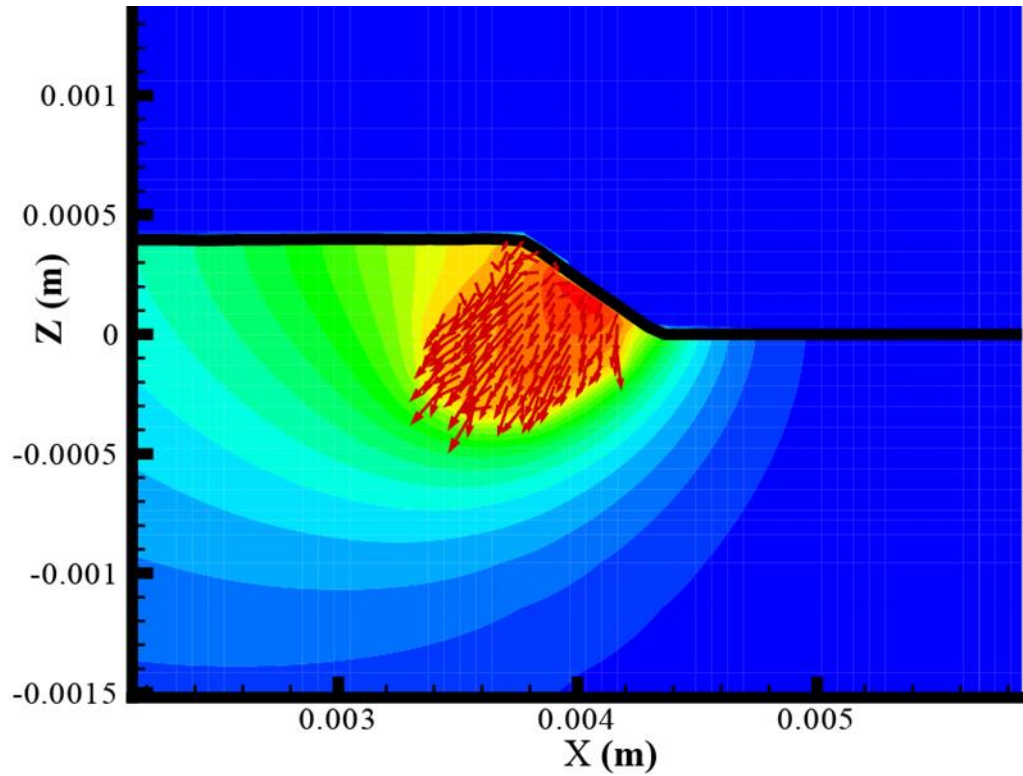


Figure 2.14 Temperature field and fluid flow in DMD process (cross sectional view of X-Z plane with 1mm-Top hat-CW-DISC laser)

To investigate the temperature change with the amount of energy, laser power is varied from 1400 Watts to 2300 Watts using a 0.5 mm TEM₀₀-CW-CO2 laser and the temperature histories with laser power are plotted in Figure 2.16. Note that proper

deposition could not be achieved by the power below 1400 Watts. Both the maximum temperature of the melt pool and the rising time increase with power, but the maximum temperature remains at 2500 Kelvin above the power of 2000 Watts.

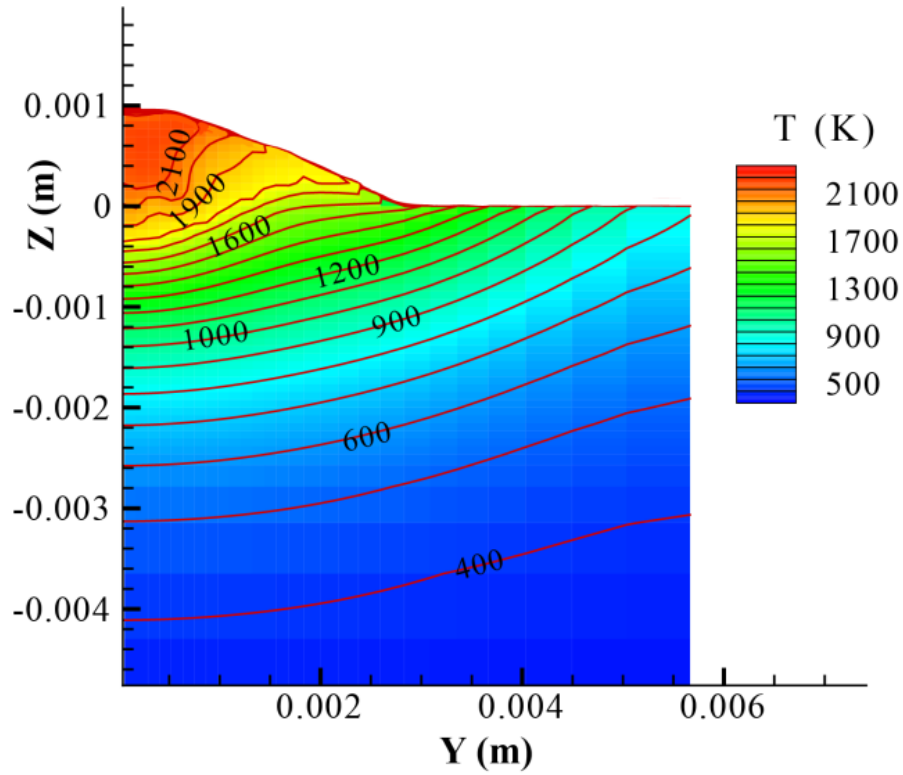


Figure 2.15 Temperature field and fluid flow in DMD process (cross sectional view of Y-Z plane with 2mm-TEM₀₁*-CW-CO₂ laser)

From the obtained temperature histories, two different cooling rates are calculated: one (CR1) is from melting temperature to austenite temperature and another (CR2) is from austenite temperature to martensite start temperature. Note that cooling rate until the ambient temperature is not shown here due to the fact that cooling rates are calculated to be compared with experimentally measured cooling rates by an infrared pyrometer and the measurable temperature range of the pyrometer is from 820 to 2800 Kelvin. As

shown in Figure 2.17, the deposition top surface has the maximum cooling rate and the cooling rate decreases as being close to the bottom of the substrate. There is a difference in cooling behavior between CR1 and CR2. At higher temperature range (CR1), the deeper the location into the substrate, the lower the cooling rate is predicted; however, at relatively moderate temperature range (CR2), the cooling rate closer to the bottom of substrate is higher by 8~9 % than that at the melt pool interface because heat transfer by conduction toward the substrate is rapid at higher temperature range, but heat transfer becomes slower as temperature drops and the heat transfer at the location away from the melt pool interface is influenced by the free surface (the bottom of substrate) at ambient temperature.

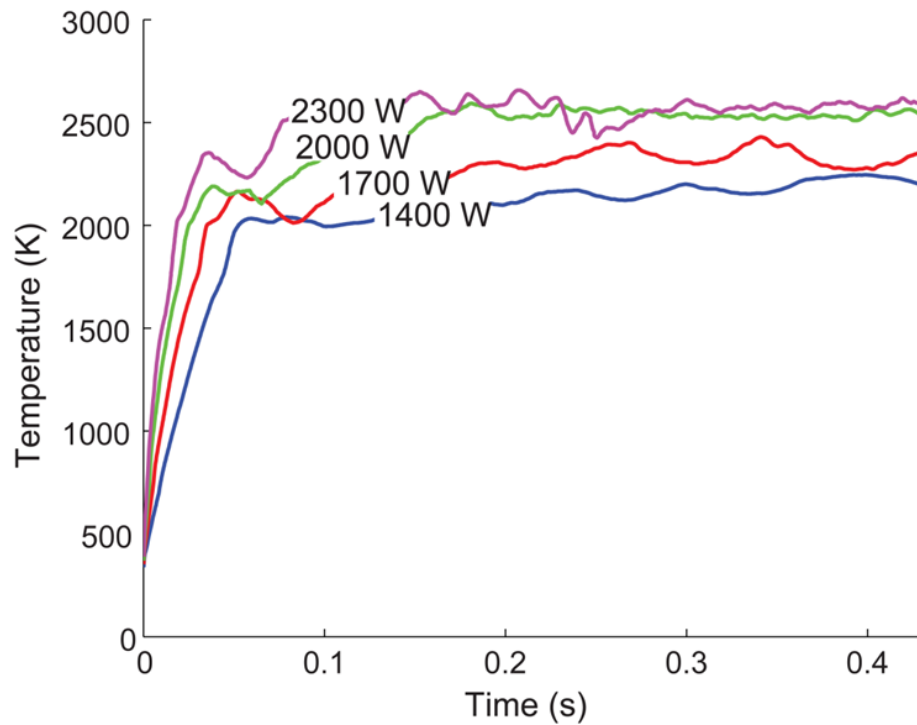


Figure 2.16 Maximum temperature of the melt pool with different laser power range from 1400 to 2300 Watts (1 mm TEM₀₀-CW-CO₂ laser)

CR1: Cooling rate (Melt T~ Aust T)
CR2: Cooling rate (Aust T~Mart start T)

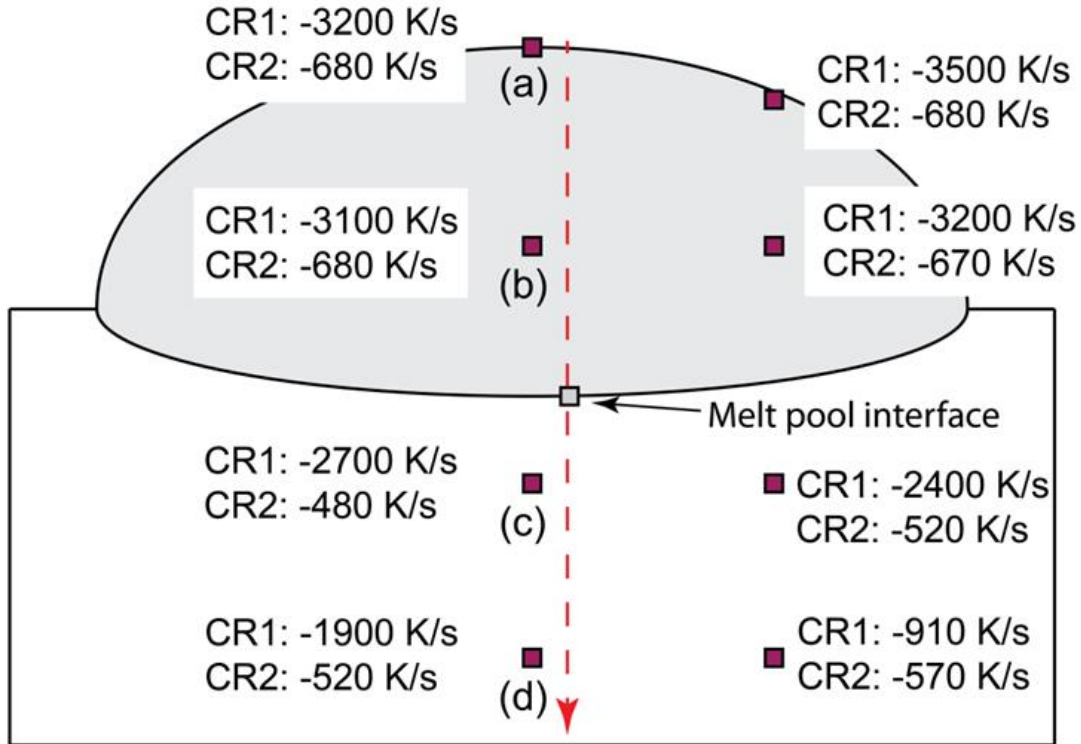


Figure 2.17 Mathematically predicted cooling rates at different locations in DMD process

The mathematically predicted solute concentrations of carbon and nickel in liquid iron solution are shown in Figure 2.18 and the Pectlet number for both elements are calculated as $3.15E4$ for carbon and $1.69E5$ for nickel by Equation 2.21, which indicates that advection transport is dominant in mass transport in DMD process and nickel element is more influenced by fluid flow than carbon.

$$Pe = \frac{\text{Advective transport rate}}{\text{Diffusive transport rate}} = \frac{Lv}{D} \quad \text{Equation 2.21}$$

where L is the characteristic length.

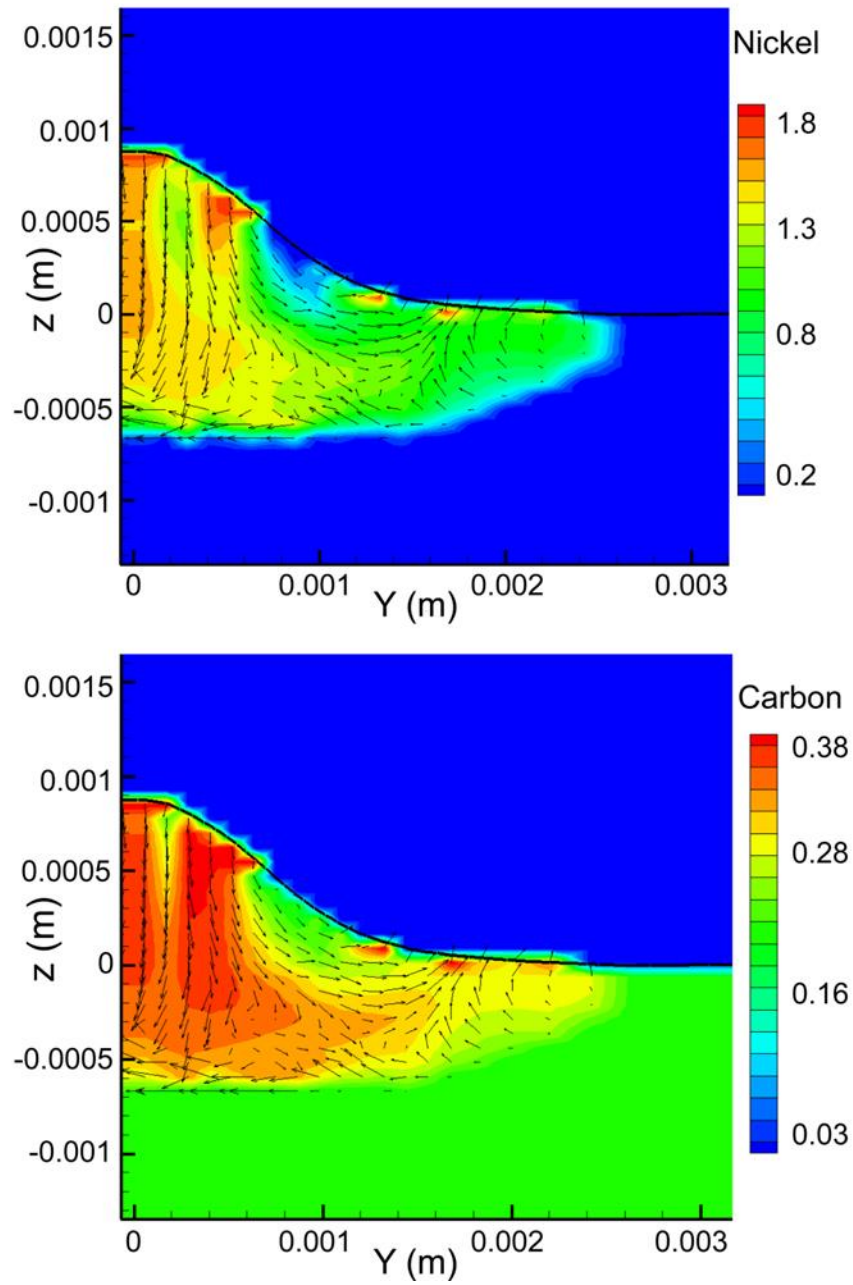


Figure 2.18 Solute transport in the laser melted pool of AISI 4340 steel: The Pectlet number for Carbon: 3.15E4 and for Nickel:1.69E5, Advective transport >> Diffusion transport

2.5.3 Effects of processing parameters on deposition geometry

Laser power and scanning speed have been varied to investigate the effects of the parameters on melt pool geometry. As shown in Figure 2.19, laser power increases the overall melt pool size with higher energy density and laser scanning speed leads to shallower penetration depth to the substrate and lower deposition height. But the deposition width relatively does not vary with scanning speed. In real DMD production line, faster scanning speed with higher amount of energy as much as possible is required for cost. To figure out the main effect of scanning speed on the deposition, scanning speed is varied with constrained energy density. An increase in interacting time between laser and a target material with slower scanning speed initially raises the deposition height with a slight increase in the width and penetration depth. However, above a certain amount of interacting time, the deposition height remains the same and the penetration depth rapidly increases which is not appropriate in real DMD applications. Providing the proper ranges of processing parameters is thus required to have a better deposition quality and lesser energy consumption.

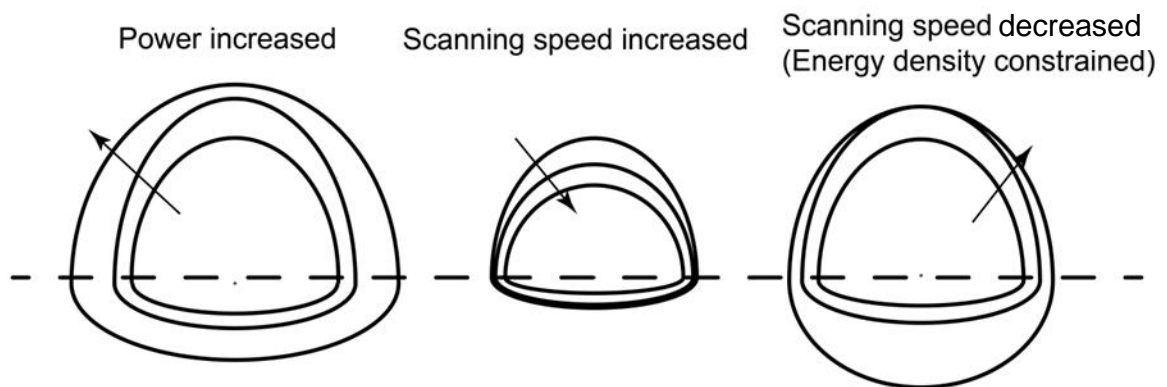


Figure 2.19 Melt pool geometry changes with processing conditions

2.6 Experimental validations

In this section, the numerical model is experimentally validated by comparing temperature history, fluid flow, and the deposition geometry (height, width, and penetration depth to the substrate) with laser power. Temperature of the material is monitored by an infrared pyrometer and the velocity of the melt pool surface is calculated from successive melt pool images taken by a high speed CCD camera during DMD process.

2.6.1 Evolution of temperature and fluid flow

An infrared pyrometer, of which spot size is 0.6 mm and the measurable temperature range is from 820 to 2800 Kelvin, is used to monitor the temperature of a melted and solidified area and the monitored temperature history is compared with the mathematical predictions. The maximum temperature is found as 2400 ± 200 Kelvin and it is greater than the numerically predicted value by 8 %, and the rising time, obtained from the minimum measurable temperature range of an infrared pyrometer to the melting temperature of AISI 4340 steel, is measured as 0.075 ± 0.032 second. The rising time predicted by the mathematical model within the same temperature range is calculated as 0.13 second, and the predicted value is greater than the experimental value by 73 %. The reason for the dissimilarity in the rising time is the fact that the pyrometer measures the maximum temperature of a selected top moving surface within the spot size (0.6 mm). Although there is a discrepancy in rising time, Figure 2.20 shows the overall temporal temperature behavior at the top surface predicted by the model is close to the experimental measurement, and the experimentally measured cooling rate from melting

temperature to austenite temperature is 3800 ± 300 K/s, which also agrees with the mathematically calculated cooling rate in Section 2.5.2.

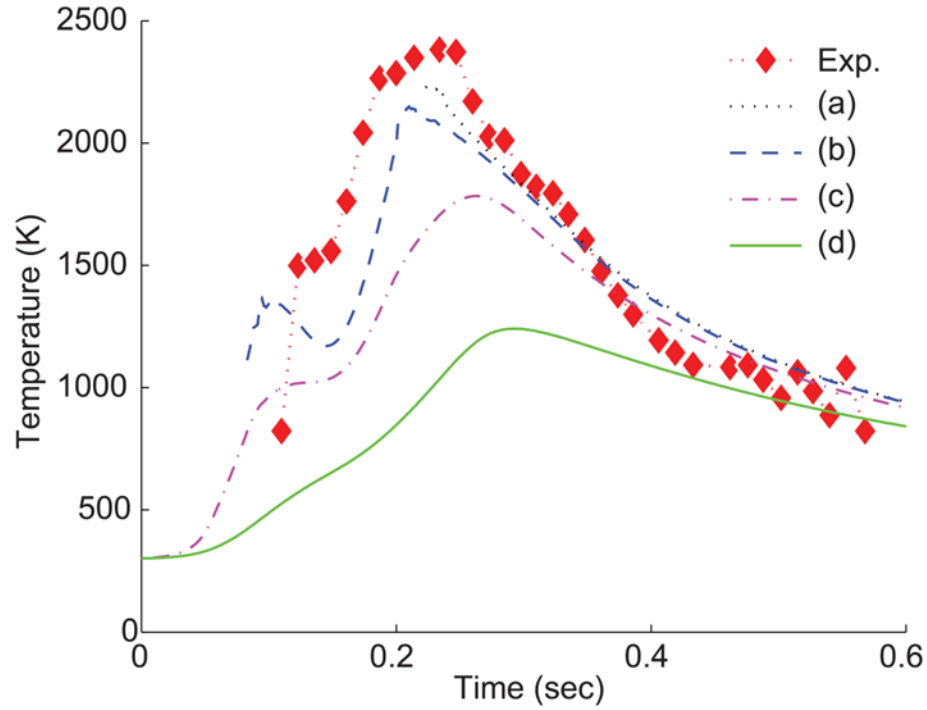


Figure 2.20 Numerically and experimentally obtained temperature history of the DMD fabricated material. The locations (a)~(d) are shown in Figure 2.17

The predicted melt pool velocity also has been validated by comparing the melt pool surface velocity that is calculated [34] by the relative motion of a hump at the melt pool surface using the successive images of melt pool taken by a high speed CCD camera as seen in Figure 2.21. An assumption used in the calculation is that the phase velocity of the wave is relatively small at the center of the hump. The calculated top surface velocity is 0.84 ± 0.19 m/s, which agrees with the mathematically predicted values 0.72 ± 0.16 m/s.

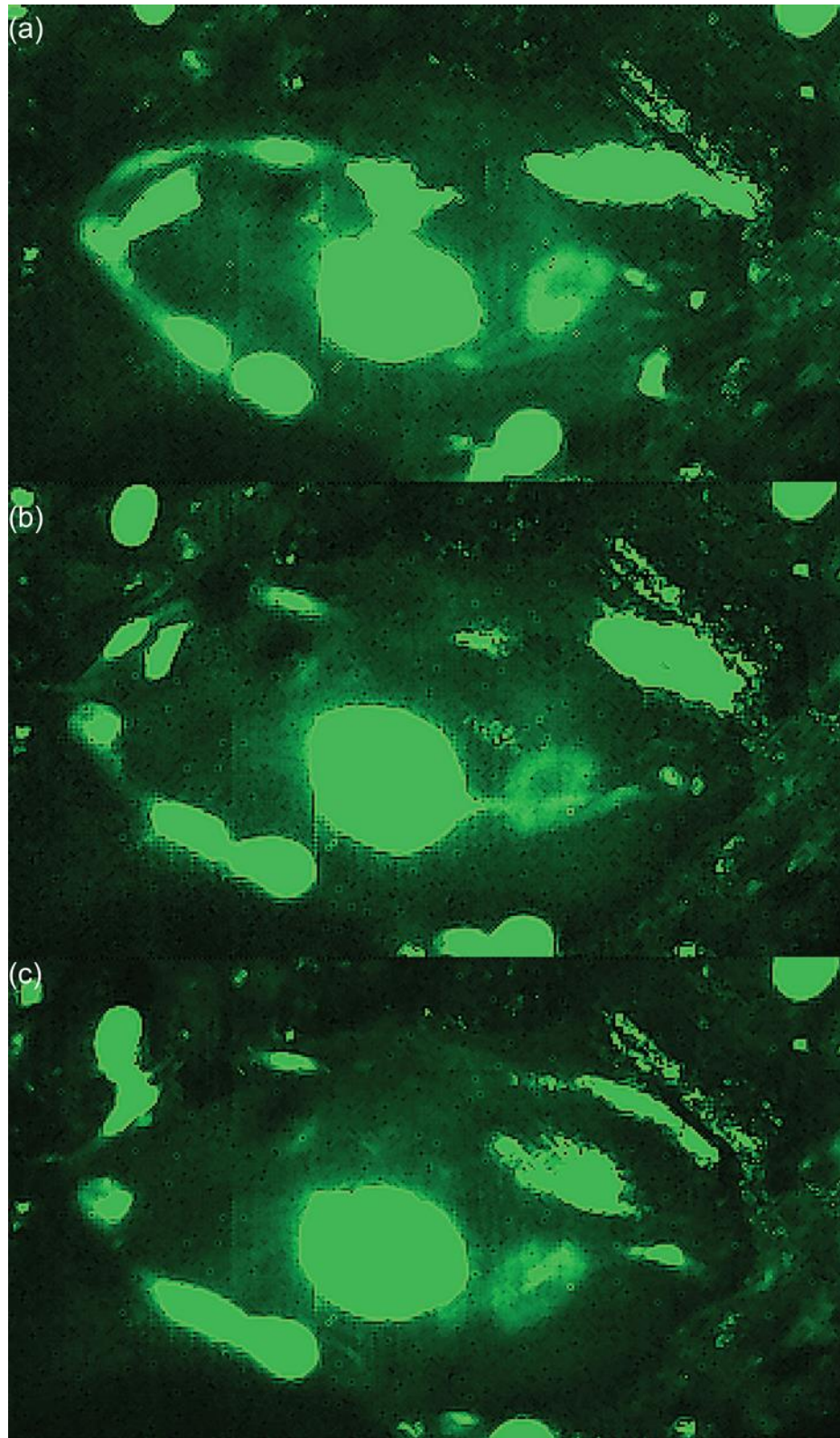


Figure 2.21 Successive images of melt pool in DMD process taken by a high speed CCD camera

2.6.2 Geometry changes with processing parameter

The deposition geometries such as height, width, and penetration into the substrate with different laser power are predicted and compared with the experimental measurements in Figure 2.22. The range of laser power simulated is from 650 W to 1300 W, and the predicted values are mostly within the experimental uncertainties. The major source of the experimental uncertainties are from replications. A few data points are slightly off from the experimental data and the discrepancies are from the fact that thermo-physical material properties at high temperature is extrapolated; however, the comparison shows that the behavior of geometry change with different power are similar and the amount of discrepancy is also small.

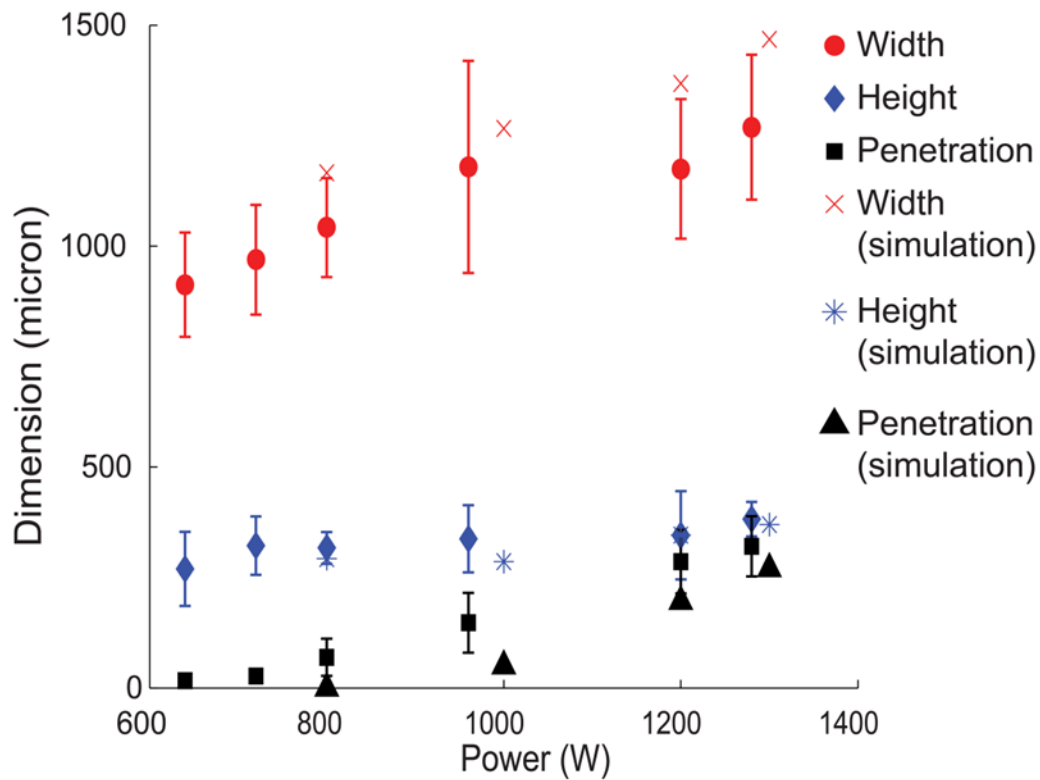


Figure 2.22 Experimental validation of melt pool geometry (width, height, and penetration to the substrate) with different laser power

2.7 Conclusions

The numerical thermal model in this chapter presented several important features of Direct Metal Deposition (DMD) process as provided below

- 1) The maximum powder temperature at the deposition surface with TEM₀₀ and TEM₀₁* mode is found where the maximum laser beam intensity is; however, the peak temperature with Top hat mode is found at the edge of beam because of the difference in distribution of laser energy and powder flow. The highest temperature of metallic powder is achieved with TEM₀₁* among the three different modes.
- 2) The uniform temperature of powder can be obtained with Top hat mode beam, which is ideal for temperature control of the laser melted area.
- 3) Temperature gradient is the highest around the melt pool interface
- 4) The maximum temperature of melt pool and the rising time ($T_{amb} \sim T_m$) increases with laser power. Above 2000 Watts with given CO₂ beam size, the maximum temperature remains the same.
- 5) Cooling rate (CR1) at high temperature range ($T_m \sim$ austenite temperature) is the highest (3500 K/s) at the top of deposition surface and CR1 decreases with deeper location toward the substrate. Cooling rate (CR2) at moderate temperature range (austenite temperature $\sim T_m$) is the highest (680 K/s) at the top of deposition surface and the cooling rate at the bottom of substrate is higher than that at the melt pool interface by 8~9 %.
- 6) Numerically obtained the Pectlet number for carbon and nickel in liquid iron solution are 3.15E4 and 1.69E5, respectively, which indicates advection due to

fluid flow generated by laser heat source is dominant in mass transport of the DMD melt pool.

- 7) The overall melt pool size increases with higher laser power and lower scanning speed. The increase in the melt pool width and penetration depth with scanning speed is relatively less than the increase in melt pool height
- 8) With constrained energy density, the longer interacting time between energy and a target material with slower scanning speed initially increases the melt pool height; however, there is a certain limit of the increase with the given beam size. Excessive interacting time leads to unnecessary diluted area.

The comparisons of temperature history, fluid flow, and the deposition geometry (height, width, and penetration depth to the substrate) with several experiments support the validity of the mathematical thermal model. The maximum temperature of the melt pool is found as 2400 ± 200 Kelvin and it is greater than the numerically predicted value by 8 %, and the rising time, obtained from the minimum measurable temperature range of an infrared pyrometer to melting temperature of AISI 4340 steel, is measured as 0.075 ± 0.032 second, which is 57 % less than the mathematically calculated rising time. Due to the fact that the pyrometer measures the maximum temperature of a selected surface within the spot size of 600 micron and the temporal temperature behaviors during cooling for both experiment and mathematical calculation are very close, we can conclude that the mathematical model is valid. The experimentally measured top surface linear velocity of AISI 4340 steel melt pool is 0.84 ± 0.19 m/s, which also agrees with the numerically obtained values 0.72 ± 0.16 m/s. Lastly, the mathematically predicted melt pool geometries with the laser power range from 650 W to 1300 W are mostly within the

experimental uncertainties. The minor discrepancy is from the fact that thermo-physical material properties are extrapolated at high temperature.

CHAPTER III

NUMERICAL MODELING: MECHANICAL DEFORMATION

MODEL

3.1 Introduction

Mechanical deformation in DMD process occurs due to severe thermal loads and solid state phase transformations such as martensitic phase transformation, and the residual stress is directly related to the fracture and fatigue behavior of the DMD fabricated product. For example, the presence of severe tensile residual stress leads to premature failure during life cycle. In situ monitoring of mechanical deformation is difficult due to the characteristic of laser material processing such that the process involves sequence of heating and melting. Therefore, the evolution of residual stress is investigated and the correlations between DMD processing parameters and the residual stress are found using a mathematical model, so that the residual stress can be controlled in the stage of constructing tool path with providing the corresponding processing variables. The obtained temporal information of temperature, geometry, and martensite formation from the model in Chapter II is imported into a commercial software package ABAQUS and the mechanical deformation in DMD process is predicted with user subroutines to include martensitic phase transformation in stress analyses.

3.2 Assumptions

The assumptions made in the mechanical deformation model in DMD process are provided below

- 1) Material is homogeneous and isotropic, and it follows Hooke's law.
- 2) Material follows Johnson-Cook plasticity model, but strain rate dependence is ignored.
- 3) Newly added element in ABAQUS for material deposition is stress-free element.
- 4) Yield stress at mushy zone is proportional to the solid fraction.
- 5) Mechanical deformation of the DMD fabricated material occurs by thermal loads and martensitic phase transformation.
- 6) Martensitic phase transformation induced plasticity is relatively small compared to the volumetric dilatation by the phase transformation [35]; therefore, only the volumetric dilatation is considered in the study for simplicity.

3.3 Boundary conditions / Constitutive model / Flow chart

The plastic behavior of AISI 4340 steel is assumed to follow Johnson-Cook hardening model and the material constants [36] are shown in Table 3.1. However, the strain rate effect on the plastic behavior is ignored for simplicity. Since DMD process involves severe thermal loads using intense laser energy within a small spot and diffusionless martensitic phase transformation, the material rapidly deforms during the process and strain rate is must be greater than the reference strain rate $\dot{\epsilon}_0$ 7500 s⁻¹, which makes the second term in the Johnson-Cook model (Equation 3.1) unity. Therefore, our assumption of the strain rate independence is reasonable.

Table 3.1 Plastic behavior of AISI 4340 steel: Johnson-Cook hardening model [36]

Johnson-Cook model	AISI 4340 steel material constants	Value
$\sigma_Y = \left[\Gamma + \Lambda (\bar{\epsilon})^z \right] \left[1 + \Pi \ln \left(\frac{\dot{\bar{\epsilon}}}{\dot{\bar{\epsilon}}_0} \right) \right] \left[1 - \left(\frac{T - T_{amb}}{T_m - T_{amb}} \right)^y \right]$ <p style="text-align: center;">Equation 3.1</p>	Γ [MPa]	2100
	Λ [MPa]	1750
	Π	0.0028
	y	0.65
	z	0.75

The total strain changes $\Delta\epsilon$ at each time step in DMD process are assumed to be thermal strain ($\Delta\epsilon^{th}$), volumetric dilatation ($\Delta\epsilon^V$) due to martensite phase transformation, and phase transformation induced plasticity ($\Delta\epsilon^{tp}$). The mechanical response due to the strain changes is decomposed into elastic ($\Delta\epsilon^e$) and plastic ($\Delta\epsilon^p$) strains. Therefore, elastic strain component can be expressed as $\Delta\epsilon^e = \Delta\epsilon - \Delta\epsilon^p$, and the elastic strain in tensor form at the end of each time step is updated as

$$\epsilon_{ij}^e = (\epsilon_{ij}^e)_t + \Delta\epsilon_{ij}^e = (\epsilon_{ij}^e)_t + \Delta\epsilon_{ij} - \Delta\epsilon_{ij}^p \quad \text{Equation 3.2}$$

Then, the stress at $t + \Delta t$ is updated with assumptions that material is homogeneous and isotropic, and it follows Hooke's law as written in Equation 3.3.

$$\sigma_{ij} = (\sigma_{ij})_t + \Delta\sigma_{ij} = (\sigma_{ij})_t + 2G \Delta\epsilon_{ij} + \lambda_L \Delta\epsilon_{kk} \delta_{ij} \quad \text{Equation 3.3}$$

where λ_L is the Lamé parameters and G is the shear modulus. If the calculated stress exceeds yield surface, the stress state is corrected by the radial return method with the plastic correction term as shown in Figure 3.1.

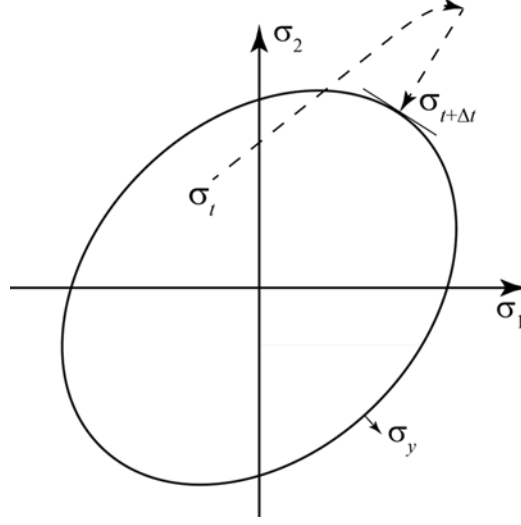


Figure 3.1 Stress state correction using radial return method

The von Mises yield surface ϕ is described in terms of effective stress σ_e , temperature T , and effective plastic strain $\bar{\varepsilon}_p$ as

$$\phi = \phi(\sigma_e, T, \bar{\varepsilon}_p) = \sigma_e - \sigma_y(T, \bar{\varepsilon}_p) \quad \text{Equation 3.4}$$

Effective stress and plastic strain are determined in terms of the deviatoric stress s_{ij} and the plastic strain increment $d\varepsilon_{ij}^p$ as seen in Equation 3.5 and 3.6, respectively.

$$\sigma_e = \sqrt{\frac{2}{3} s_{ij} s_{ij}} \quad \text{Equation 3.5}$$

$$\bar{\varepsilon}_p = \int_0^t \left(\sqrt{\frac{2}{3} d\varepsilon_{ij}^p d\varepsilon_{ij}^p} \right) dt \quad \text{Equation 3.6}$$

The plastic strain grows in parallel with the normal to the yield surface and the plastic multiplier dp , the magnitude of the plastic strain, is obtained by solving a non-linear equation derived from the consistency condition as

$$\phi + \left(\frac{\partial \phi}{\partial \sigma_{ij}} \right) d\sigma_{ij} + \left(\frac{\partial \phi}{\partial T} \right) dT + \left(\frac{\partial \phi}{\partial \bar{\varepsilon}^p} \right) d\bar{\varepsilon}^p = 0 \quad \text{Equation 3.7}$$

The obtained plastic multiplier is then used to calculate the plastic strain increment as

$$d\varepsilon_{ij}^p = dp \frac{\partial \phi}{\partial \sigma_{ij}} \quad \text{Equation 3.8}$$

The thermal strain increment due to thermal loads is expressed in terms of temperature and temperature-dependent thermal expansion coefficient α (See Equation 3.9), and temperature dependent thermal expansion coefficient for AISI 4340 steel [24] is shown in Figure 3.2

$$d\varepsilon_{ij}^{th} = \alpha dT \delta_{ij} \quad \text{Equation 3.9}$$

The volumetric dilatation due to martensitic phase change is calculated by

$$d\varepsilon_{ij}^v = \delta_{ij} \frac{\Delta V_{\gamma \rightarrow m}}{3V_0} dV_m \quad \text{Equation 3.10}$$

where V_0 is the volume at the end of the previous time step, $\Delta V_{\gamma \rightarrow m}$ is the volume change due to phase transformation from austenite to martensite, and dV_m is the amount of martensite phase change.

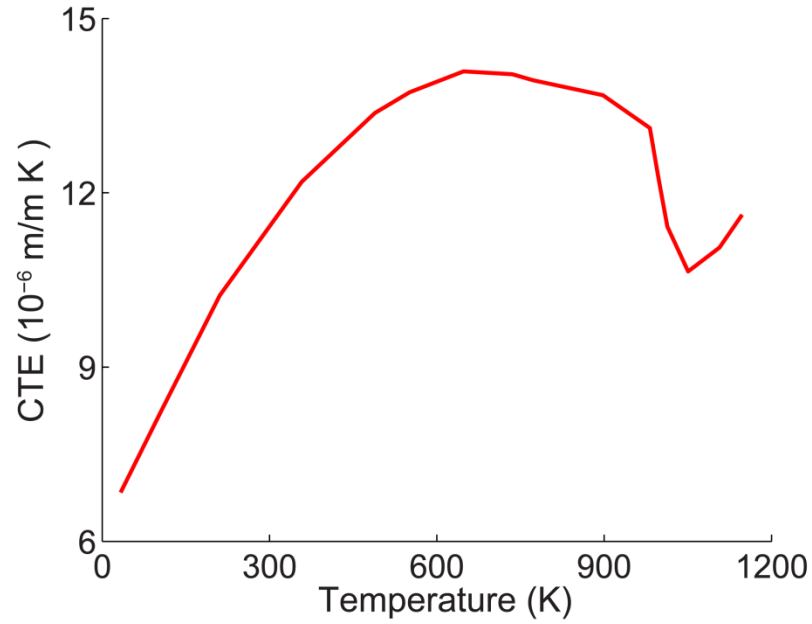


Figure 3.2 Temperature dependent coefficient of thermal expansion (CTE) for AISI 4340 steel [24]

The transformation induced plastic strain is proportional to stress field and the plastic strain can occur although stress is below the yield limit. Transformation plastic strain increment [37-39] is obtained by

$$d\varepsilon_{ij}^{tp} = \frac{5\Delta V}{4V\sigma_y} s_{ij} (1 - V_m) \frac{dV_m}{dt} \quad \text{Equation 3.11}$$

However, in martensitic phase transformation induced mechanical deformation, the volumetric dilatation is dominant [35] compared to transformation induced plasticity. Therefore, the martensite transformation induced plasticity is not included in this study to reduce computational costs.

Since material is melted and solidified in the process, stress-free element is used in ABAQUS to account for the material deposition and yield stress is proportionally assigned by solid volume fraction at mushy zone. If the fraction of liquid is greater than 50 %, the element is removed in numerical calculation. The overall flow chart of the mechanical deformation model in DMD process is shown in Figure 3.3.

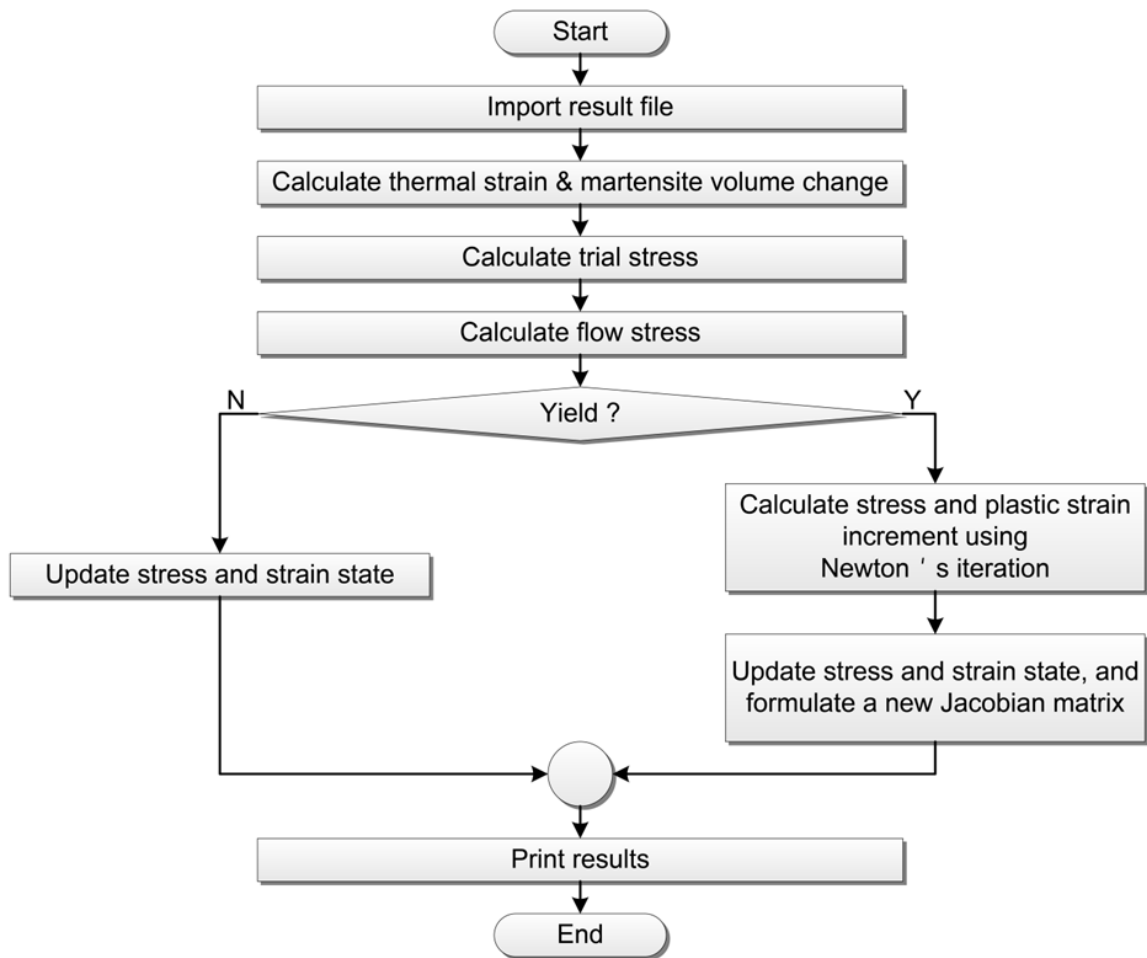


Figure 3.3 Flow chart of mechanical deformation model in DMD process

3.4 Martensitic phase transformation in laser material processing

Solid state phase transformations occur in order to lower the energy of the system during cooling. Typical carbon steel becomes austenite phase (γ) as heated above austenite temperature and it transforms into different structures with cooling. If cooling rates are rapid enough to avoid the pearlitic and bainitic phase transformations as in laser material processing, the carbon atoms in the austenite phase do not have sufficient time to diffuse and the austenite is distorted by the trapped carbon, which is diffusionless phase transformation. In laser deposition of AISI 4340 steel, the laser melted material cools down from the austenite (F.C.C. structure) temperature with a cooling rate above 670 K/s, which is higher than the critical cooling rate (625 K/s) of AISI 4340 steel [40]; therefore, all the melted and solidified materials (F.C.C.) fully transform into martensite (B.C.T.) without F.C.C. to B.C.C. transformation. The previous study [41] in CLAIM also showed that the AISI 4340 steel deposited by a fiber coupled diode laser has more than 95% of martensite and the rest phases are the retained austenite, and cementite. In this study, a 1.0 mm-CW-Top hat-DISC laser is used to deposit a single AISI 4340 steel layer and the entire deposited region have martensite as seen in the scanning electron microscopic images (Figure 3.4). The specific volume of martensite is 4% higher than that of F.C.C structure [42]; therefore, martensitic phase change should be accommodated in the mechanical deformation model in laser aided material processing, especially for carbon steel fabrication. This has been done by using user subroutines in ABAQUS.

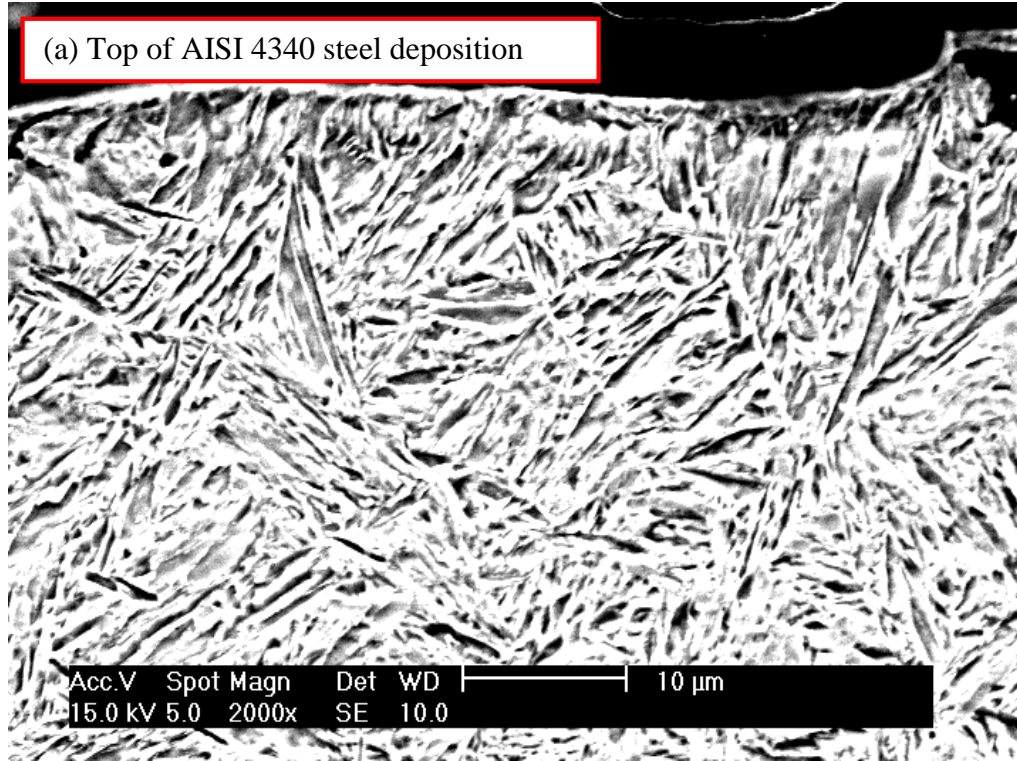
The martensite volume fraction of the material is predicted by the empirical relationship made by Koistinen and Marburger [43] as expressed in Equation 3.12.

$$V_m = 1 - \exp[-0.11 \cdot (M_s - T)] \quad (T < M_s) \quad \text{Equation 3.12}$$

where M_s is the martensite transformation start temperature, which is predicted by alloying composition of AISI 4340 steel [44]

$$M_s (^\circ\text{C}) = 512 - 453 \cdot C - 16.9 \cdot \text{Ni} + 15 \cdot \text{Cr} - 9.5 \cdot \text{Mo} \\ + 217 \cdot (C)^2 - 71.5 \cdot (C)(\text{Mn}) - 67.6 \cdot (C)(\text{Cr}) \quad \text{Equation 3.13}$$

Note that rapid cooling with laser aided material processing leads to fine grain size, which depresses M_s ; however, this is not considered in the study.



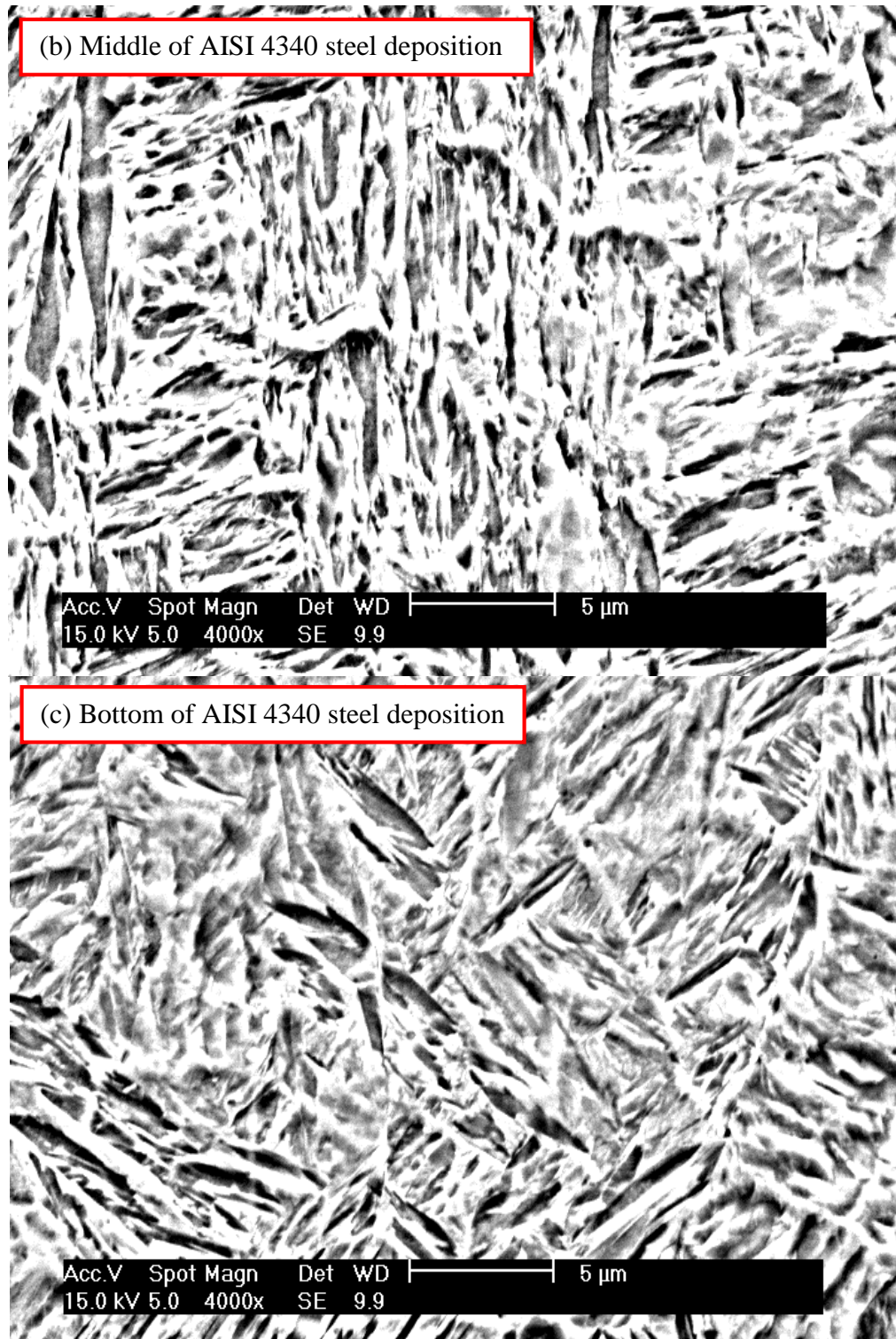


Figure 3.4 Martensite is found in AISI 4340 steel deposition using 1.0 mm-Top hat- CW-DISC laser: (a) Top (b) Middle (c) Bottom region of a single layer deposition

Since the Koistinen and Marburger's empirical model is not a function of cooling rate, the Avrami's empirical model [45], expressed in Equation 3.14, is accompanied with the martensitic phase transformation model. We assumed that there is no diffusive phase transformation within the martensitic phase transformation temperature range ($M_s \sim M_f$) and there is only one type of diffusive phase transformation, pearlite phase transformation from melting temperature to martensite start temperature.

$$V_p = 1 - \exp(-mt^n) \quad \text{Equation 3.14}$$

in which V_p is the volume fraction of a newly created pearlite phase from austenite, and m and n are the material constants. The constants can be extracted from a time-temperature transformation diagram at some points; then, the extracted material constants m and n are curve-fitted to obtain the temperature dependent constants for a temperature range of interest. For non-isothermal phase transformation, the authors [46] developed a fictitious time t^* and volume fraction f^* using the Avrami's model as

$$t_j^* = \left[-\frac{\ln(1 - f_{j-1})}{m_j} \right]^{1/n_j} \quad \text{Equation 3.15}$$

$$f_j^* = 1 - \exp \left[m_j (t_j^* + \Delta t)^{n_j} \right] \quad \text{Equation 3.16}$$

Then, the total volume fraction of a new phase f in non-isothermal cases can be calculated by

$$f = f_j^* (f_{j-1}^\gamma + f_{j-1}) f_{\max} \quad \text{Equation 3.17}$$

where the subscript j and $j-1$ represent the end of current and previous time step, respectively.

The volume fraction of each phase in a single AISI 4340 steel (610 micron height) layer is calculated and shown in Figure 3.5. As seen in the experimental results (Figure 3.4), the entire deposited (melted and solidified) materials fully transform into martensite, and the martensite is also partially found below 350 micron from the melt pool interface in heat affected zone.

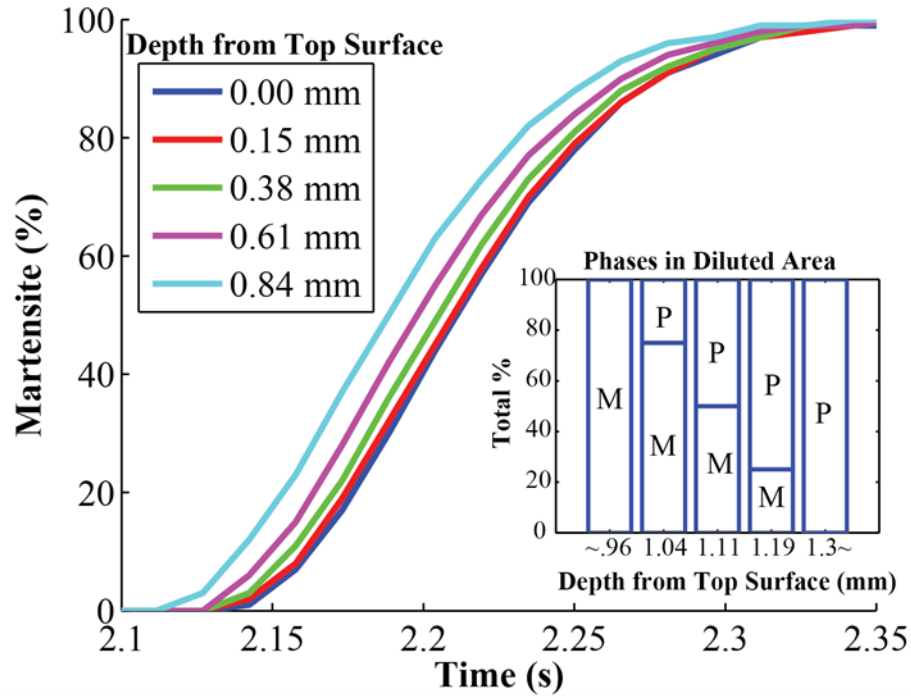


Figure 3.5 Numerically calculated volume fraction of metallurgical phases (Martensite and Perlite) at different locations with 1.0 mm-Top hat-CW-DISC laser

3.5 Evolution of residual stress in DMD process

In this section, the numerically predicted temperature history and metallurgical phase information are imported into a commercial software package ABAQUS with user subroutines and the model has been used to investigate the evolution of the residual stress. It should be noted that the magnitudes of all the shear stresses are relatively small compare to the normal stress components; therefore, all the conclusions are made based on the behaviors of the normal stress components.

Figure 3.6 and 3.7 show the evolution of the residual stress in longitudinal (scanning direction) and transverse direction, respectively, of a single layer deposition. The material is thermally expanded with laser heat source and the expanded materials compress the thermally unaffected neighboring elements. As a consequence, compressive stress is created at the material ahead of laser beam scanned area. As the beam is approaching to the compressed area, the compressive stress is accumulated by heating and the peak value is found as close as the yield strength at the top surface of the substrate. The longitudinal and the transverse stress components have their own peak compressive stress at the center of the scanning line and the edge of the beam-scanned area, respectively. The compressive stress formed by the thermal expansion decreases or becomes zero if the material is close to the melted area because mechanical deformation is recovered by the neighboring melted region: the magnitude of the alleviated compressive stress is greater as closer to the melt pool interface. The melted material is solidified and contracted with a cooling rate above 3000 K/s, which creates relatively high tensile stress. The thermally affected but un-melted material below the interface is not only contracted itself by conduction cooling but also affected by the more rapidly

cooled layers above the interface. As a result, the deposited (melted and solidified) material and the material close to the melt pool interface have the tensile residual stress, and the peak value is found near the interface: the peak values in S_{xx} and S_{yy} direction are found at the center of the scanning line and the edge of the deposited area, respectively. The amount of tensile stress is decreasing along the Z axis below the interface and the compressive residual stress is eventually found (about 300 micron below the interface), which was created during the heating stage mentioned above.

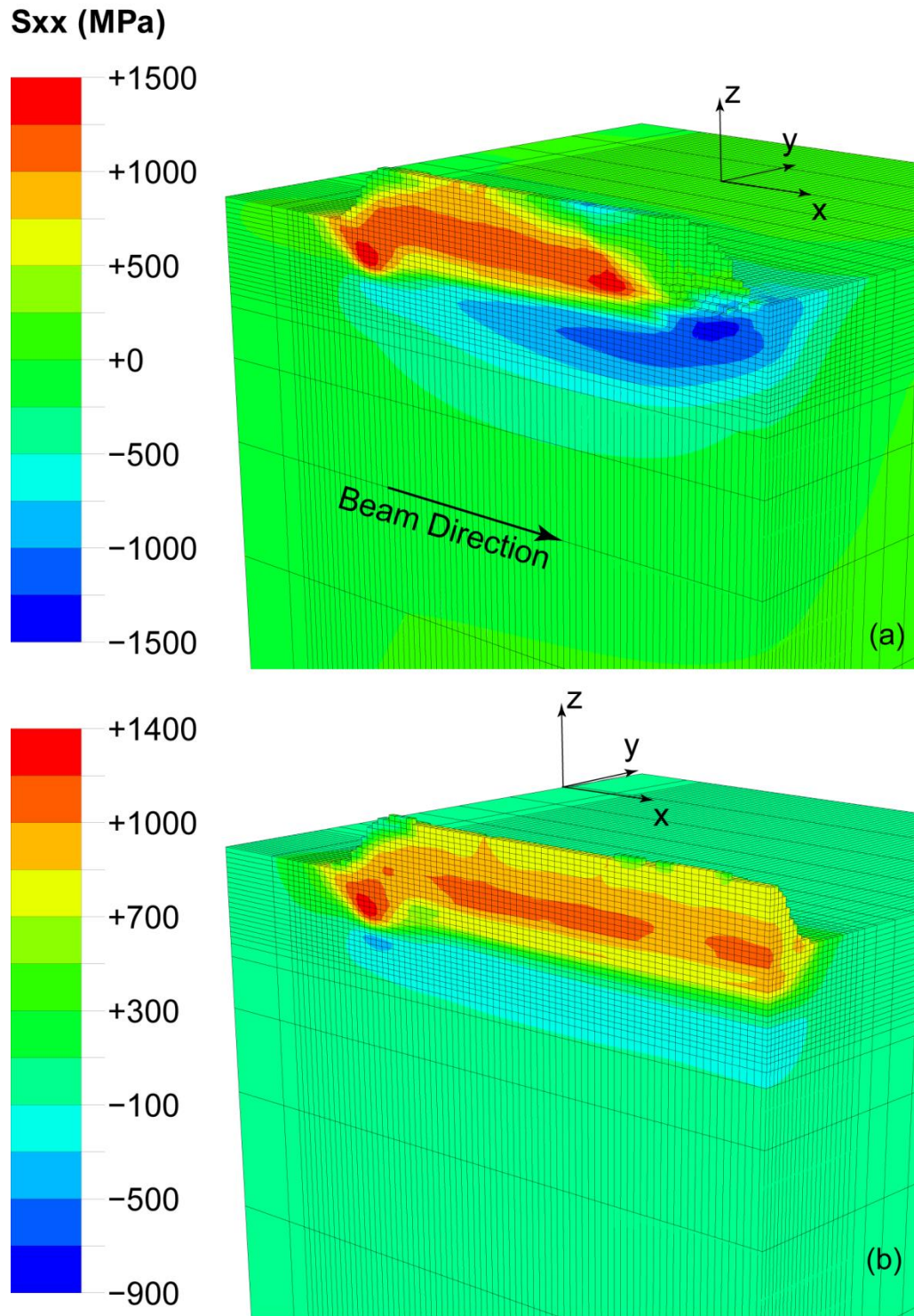


Figure 3.6 Transient (a) and residual stress (b) in longitudinal (beam scanning) direction of a single AISI 4340 steel layer deposition

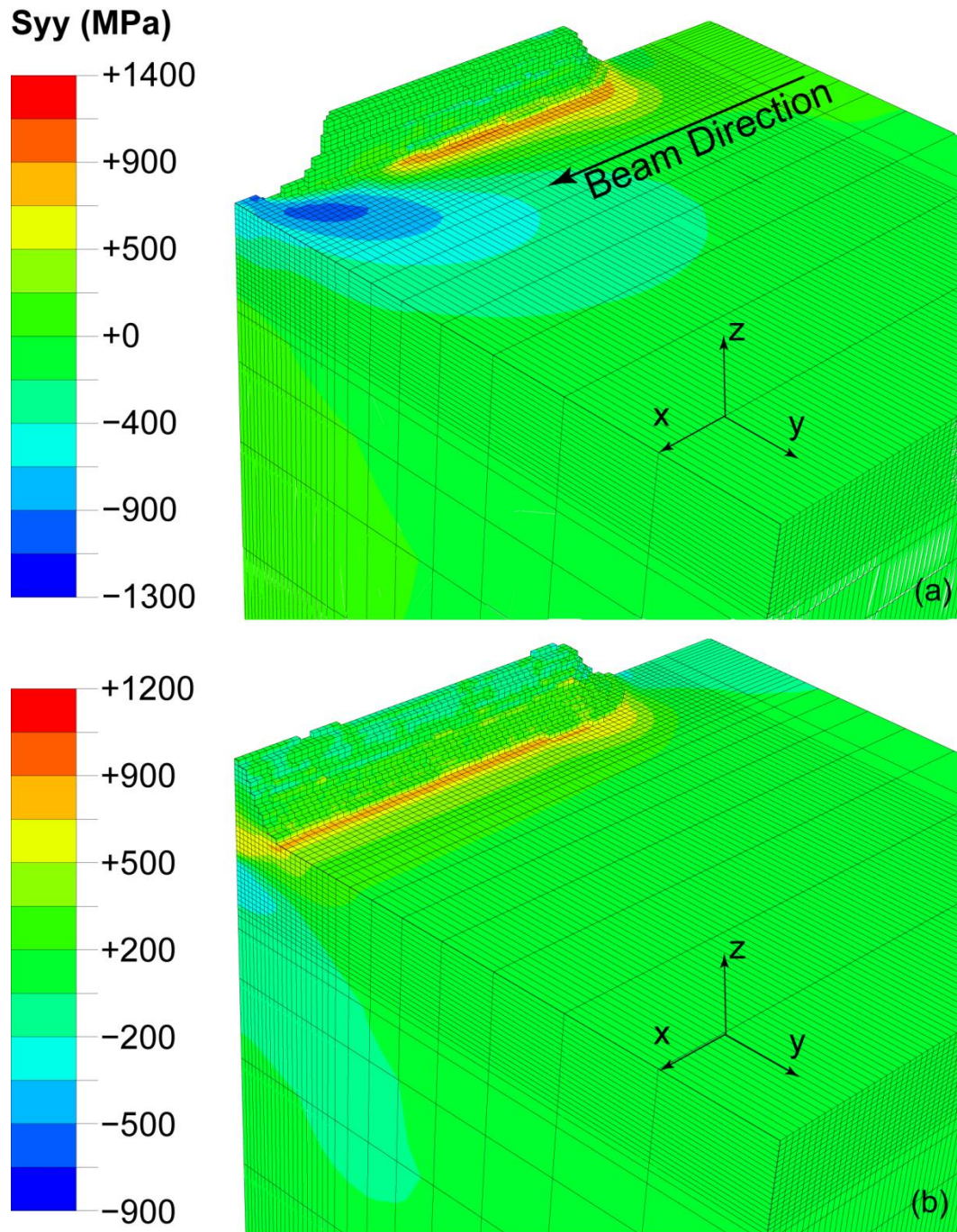


Figure 3.7 Transient (a) and residual stress (b) in transverse direction of a single AISI 4340 steel layer deposition

In order to further investigate the evolution of the mechanical deformation near the melt pool interface, the normal stress components above and below the interface are plotted with temperature in Figure 3.8. The compressive stress in S_{xx} direction starts developing due to the thermally expanded neighboring layers even before it is thermally affected. On the other hand, a relatively small amount of tensile stress is initially created in S_{yy} direction, but the stress rapidly becomes in compressive state as the temperature of the selected region starts rising. The stress component in S_{zz} direction follows the similar behavior as the S_{xx} stress, but the magnitude of the stress is relatively smaller than other two normal components; therefore, the detailed explanation of the S_{zz} stress component is not presented. The state of stress above the melt pool interface, where the material experiences melting / solidification during the process, is zero-stress when the material starts being solidified and contracted; therefore, the magnitude of the residual stress above the interface should be greater in tensile direction than that below the interface, of which the stress is in compressive state before contraction. This concludes that the initial state of the stress before cooling plays a great role to determine the final state of the residual stress. If melting did not occur, the mechanical deformation is always the same with the constrained energy input; however, due to the fact that DMD process involves melting and it alleviates the mechanical deformation during the process, the residual stress can be altered by different melt pool geometry / location with different processing conditions even with the same amount of energy density.

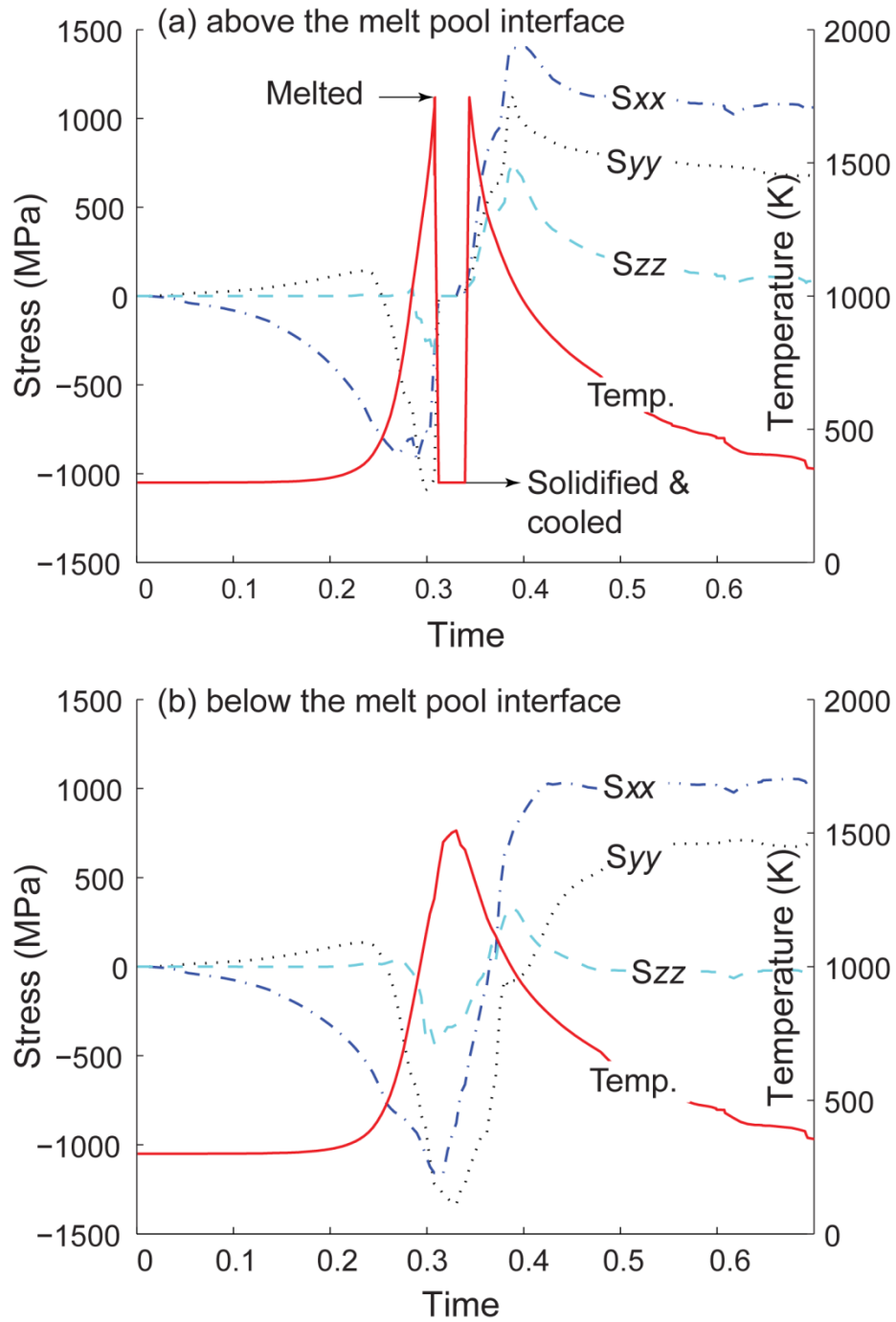


Figure 3.8 Evolution of residual stress with temperature: (a) above the melt pool interface
(b) below the interface

3.6 Effects of volumetric dilatation due to martensite phase transformation

In order to examine the effect of martensite on the residual stress of the bulk material and to compare with the experimental measurements, the residual stress in S_{xx} direction are averaged within the deposition width and plotted along the Z axis as shown in Figure 3.9. The fully transformed martensite is found until 200 micron below the melt pool interface and the magnitude of the tensile residual stress above the martensite transformation zone is reduced with the volumetric dilatation. Two of areas above and below the melt pool interface are selected and the mechanical deformation histories with and without martensitic phase transformation are plotted in Figure 3.10 to explore how the residual stress in S_{xx} (laser scanning) direction at the melt pool interface is altered by martensitic phase transformation. The amount of the reduction in the residual stress due to the volumetric dilatation above the interface is greater than that below the interface because the upper area has more martensite around it. Martensitic phase transformation during cooling leads to the compressive residual stress due to the volumetric dilatation as observed in other authors' studies [12-14, 35]; however, this study shows that the tensile residual stress exists even with fully transformed martensite because the residual stress is determined not only by the amount of the transformed martensite around the area but also by the initial state of the transient stress before martensitic phase transformation starts.

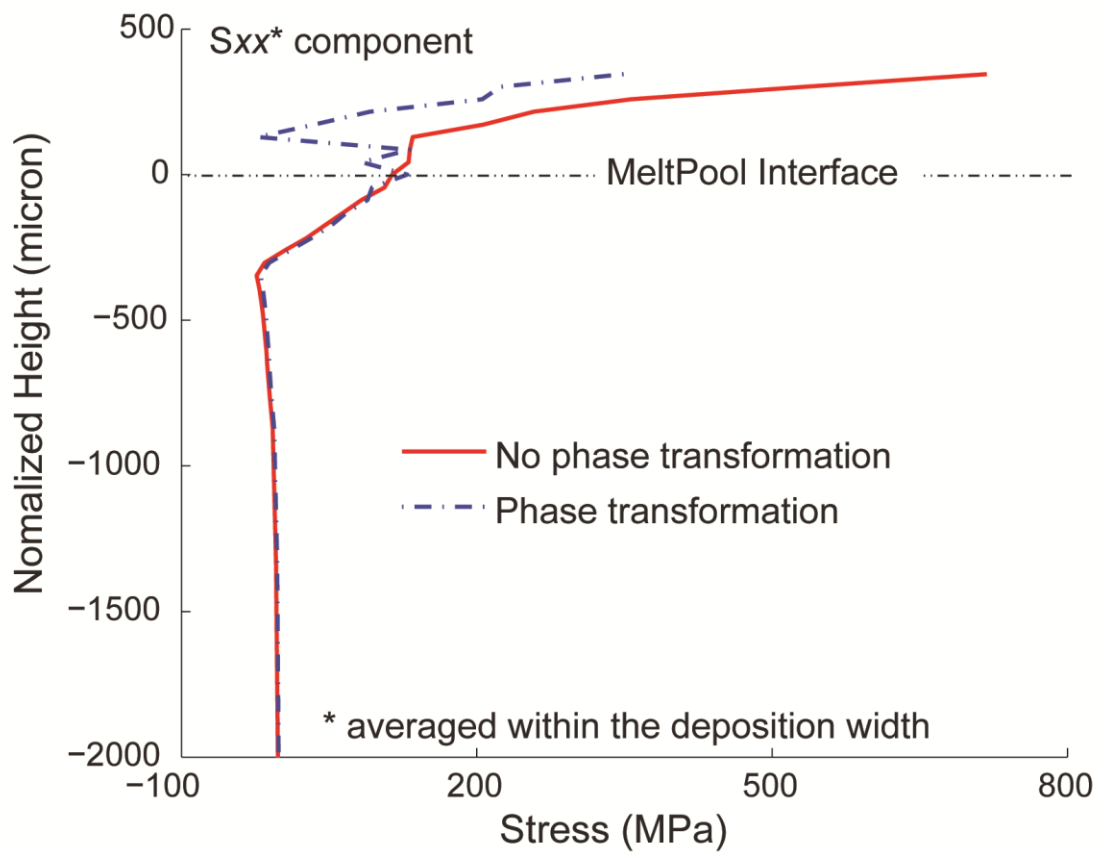


Figure 3.9 Martensite phase transformation effects on the residual stress profile along the Z axis (the dashed down arrow in Figure 2.17 shows the region where the residual stress profile is made) Note that S_{xx}^* is the averaged residual stress within the deposition width.

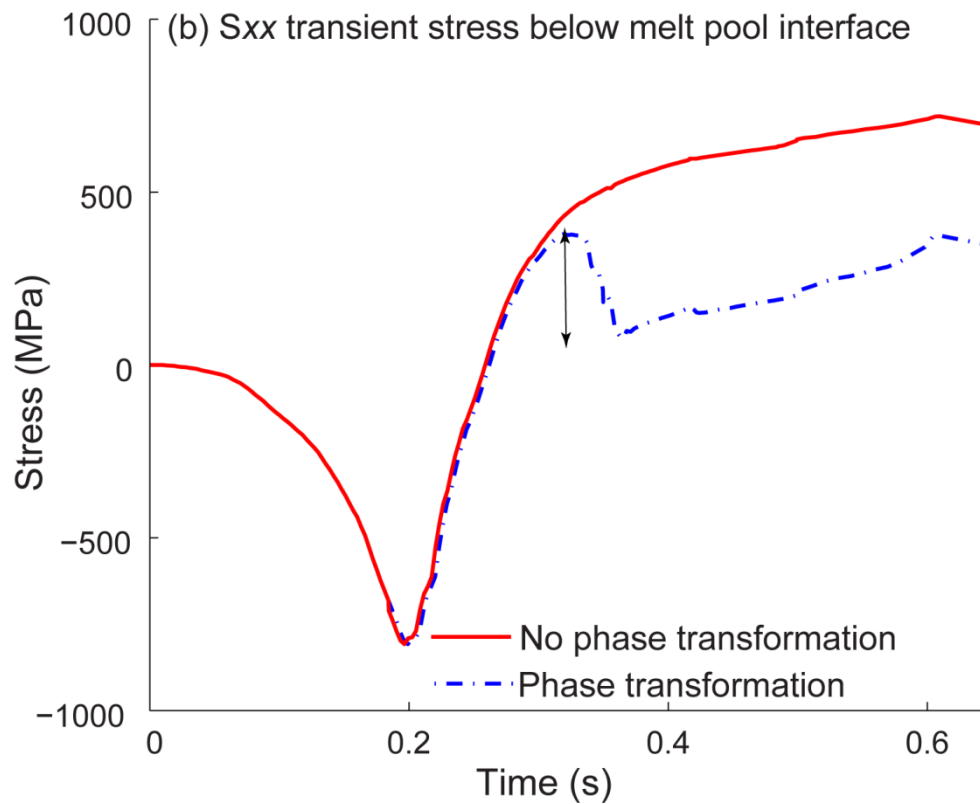
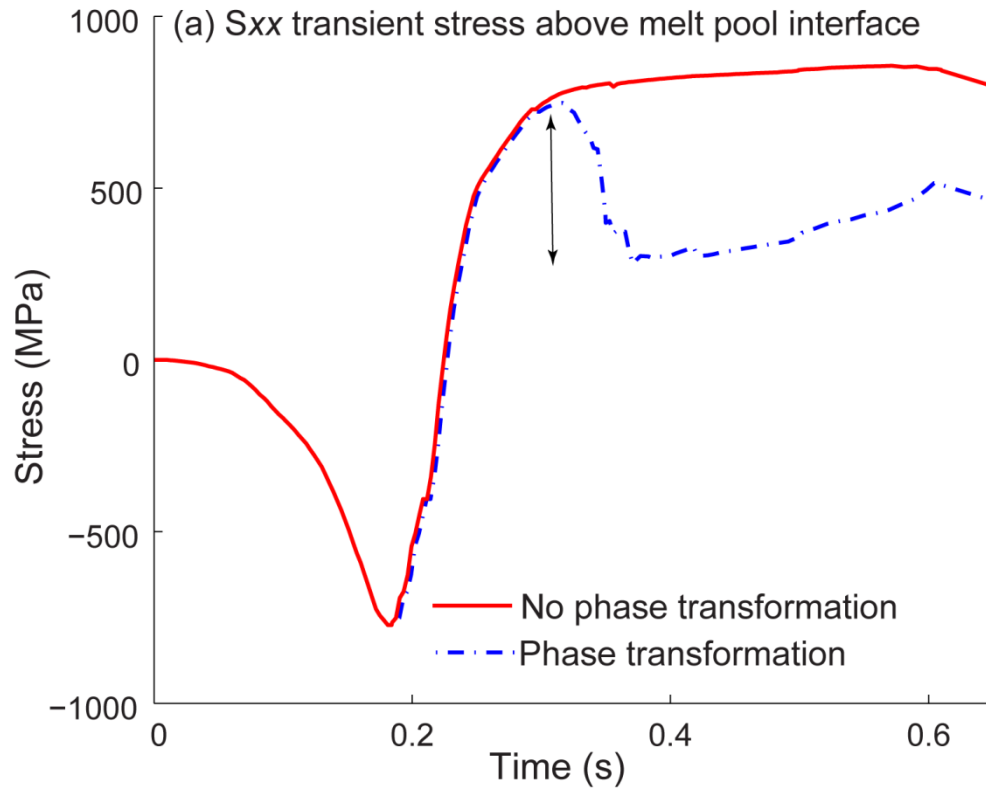


Figure 3.10 Evolution of S_{xx} stress component near the melt pool interface with and without martensite phase transformation: (a) above the interface (b) below the interface

3.7 Experimental validations: X-ray diffraction residual stress measurement

X-ray diffraction residual stress measurements are conducted at the top surface and the melt pool interface of the AISI 4340 steel deposited sample (Irradiated area: 5.1 x 0.5mm) using a two-angle sine-squared-psi technique employing the diffraction of chromium $K\alpha$ radiation from the (211) planes of the BCC structure of the sample, and the measurements are compared with the numerically calculated residual stress to validate the mathematical models. The diffracted intensity, peak breadth, and position of the $K\alpha$ 1 diffraction peak are determined by fitting the Pearson VII function peak profile [47]. The incident beam divergence is 1.0 degree, and Psi rotation angles are 10.0 and 50.0 degree. For subsurface residual stress measurement, the material on the top of the sample is electrolytically removed to minimize the change in residual stress with material removal. The residual stress is calculated from the obtained strain by employing the X-ray elastic constant of AISI 4340 steel in accordance with ASTM E1426.

The mathematically predicted residual stresses within the chromium $K\alpha$ irradiated area are averaged and compared with the experimental measurements as shown in Table 3.2. The numerically obtained residual stresses at the top surface and the melt pool interface are greater than the experimentally characterized values by 8.6 ± 5.6 % and 35.7 ± 11.6 % respectively. The main reason for the discrepancies between the residual stresses is the extrapolated thermo-physical material properties of AISI 4340 steel at high temperature due to the limitation of an access in database. The discrepancy of the residual stress at the subsurface is greater than that at the top deposition surface because of the material removal for subsurface residual stress measurement. However, we can conclude

that the numerical models well predicts the residual stress of the DMD fabricated coupon due to the facts that the behavior of the residual stress from the top surface to the melt pool interface is very similar and the residual stresses are in the same order and direction.

The (211) diffraction peak width is indication of how the material has been processed and the depth to which it has been plastically deformed. In work hardening materials, the diffraction peak width increases with work hardening by plastic deformation. The diffraction peak width at the melt pool interface is higher than that at the top surface, which represents the material at the interface is harder than the material at the top surface. The equivalent plastic strains at the surface and the melt pool interface from the numerical model are 5.4E-3 and 14.4E-3, respectively, which also shows that the material at the interface is more work hardened in DMD process.

Table 3.2 Longitudinal (S_{xx}) residual stresses of a single DMD layer of AISI 4340 steel

	Top surface	Melt pool interface
Experimentally measured residual stress (MPa)	319±18	129±15
Numerically predicted residual stress (MPa)	349	83
The (211) diffraction peak width (deg.)	3.85	4.26

3.8 Conclusions

Residual stress analyses in this chapter present the evolution of residual stress in Direct Metal Deposition (DMD) process and the effects of martensitic phase transformation on the residual stress. The important findings are provided below

- 1) All the shear stresses are relatively small compared to the normal stress components. Among the three normal components, S_{xx} direction (beam scanning direction) residual stress is dominant and S_{zz} direction residual stress is relatively small.
- 2) There are three stages to determine the final state of the residual stress in DMD process:
 - a. Heating: compressive state
 - b. Melting: relieving
 - c. Cooling: tensile state

Material experiences compressive stress due to the thermally expanded neighboring layers with a laser heat source, all the accumulated compressive stress is alleviated by melting, and the residual stress is built up with solidification and cooling. If martensitic phase transformation exists, the residual stress is reduced toward compressive direction by the volumetric dilatation. The amount of reduction depends on the amount of surrounded martensite and the initial stress state before martensite phase starts transforming.

- 3) The peak residual stresses in S_{xx} and S_{yy} direction are found at the center of the scanning line and the edge of the deposited area, respectively.

- 4) Different melt pool geometry and location with altering processing parameters lead to different residual stress field in DMD process

X-ray diffraction residual stress measurement supports the validity of the mechanical deformation model. The mathematically obtained residual stresses at the top surface and the melt pool interface are greater than the experimentally characterized values by 8.6 ± 5.6 % and 35.7 ± 11.6 % respectively. The greater discrepancy at the melt pool interface is from the fact the material has to be removed for the subsurface residual stress measurements. The mathematically calculated equivalent plastic strains at the top surface and subsurface are 5.4×10^{-3} and 14×10^{-3} , respectively, and the (211) diffraction peak width (top surface: 3.85 and subsurface: 4.26) supports that the material at the melt pool interface is more plastically deformed than at the top surface.

CHAPTER IV

CORRELATIONS OF PROCESSING CONDITIONS

4.1 Introduction

In this chapter, key DMD processing parameters, such as metal powder flow rate, laser power, scanning speed, scanning direction, and the number of layers for a given deposition height, are varied within the range that results in the suitable deposition quality to investigate the effects of processing parameters on the residual stress, which can be utilized in the stage of building tooling path for a required residual stress profile. The study in this chapter only includes thermal strains as a boundary condition to figure out the main effects of the processing variables. The effect of martensite is explained in Chapter 3.6: the magnitude of the tensile residual stress at the laser deposited region decreases depends on the amount of martensite around it. Note that the maximum tensile residual stress in S_{yy} direction is found at the edge of the deposited area as described in Chapter 3.5. Since multiple metal layers are normally deposited with overlapping in DMD process, the considerable residual stress at the edge will be recovered by re-melting with the adjacent layer deposition; therefore, the transverse residual stress at the deposition edge is not a major concern in real DMD applications. On the other hand, the presence of the significant tensile residual stress at the center of the scanning line around

the melt pool interface could lead to premature failure during life cycle. Accordingly, this study focuses on the residual stress at the center of the scanning line, and the residual stress profiles along the Z axis with different processing variables are plotted in Figure 4.1-4.3, and 4.6 to investigate the processing parameter effects in the residual stress. Note that the residual stress profiles are normalized in terms of the location of the melt pool interface because different processing parameters lead to different penetration depth of the melt pool into the substrate and the residual stress profile is distinguished by the penetration depth.

4.2 Metallic powder flow rate

Figure 4.1 shows the residual stress profiles along the Z axis with the powder flow rate of 4.7 and 6.3 grams per minutes. The increased powder flow rate does not change the size of the melt pool, especially the height, because the amount of energy given is constrained with the constant laser power and scanning speed. However, the entire melt pool sinks downward toward the substrate with lesser powder flow rate. Due to the independence of the melt pool size on the powder flow rate, this study separates the penetration depth effects on the residual stress from other effects such as the amount of the energy used and the melt pool size. The peak residual stress locations are not changed by the penetration depth with different powder flow rate: the maximum tensile and compressive stresses are found at the melt pool interface and 600 micron below the interface, respectively, which suggests that the amount of energy density delivered into the material plays the main role in determining where the peak residual stresses are. However, the shallow penetration to the substrate with a higher powder flow rate reduces the magnitude of the residual stress in both tensile and compressive directions because

the shallow penetration alleviates less the amount of the compressive stress built by the thermal expansion of the neighboring layer during heating stage as mentioned in Chapter 3.5; that is, more material starts being contracted from the compressive stress state with a higher powder flow rate. .

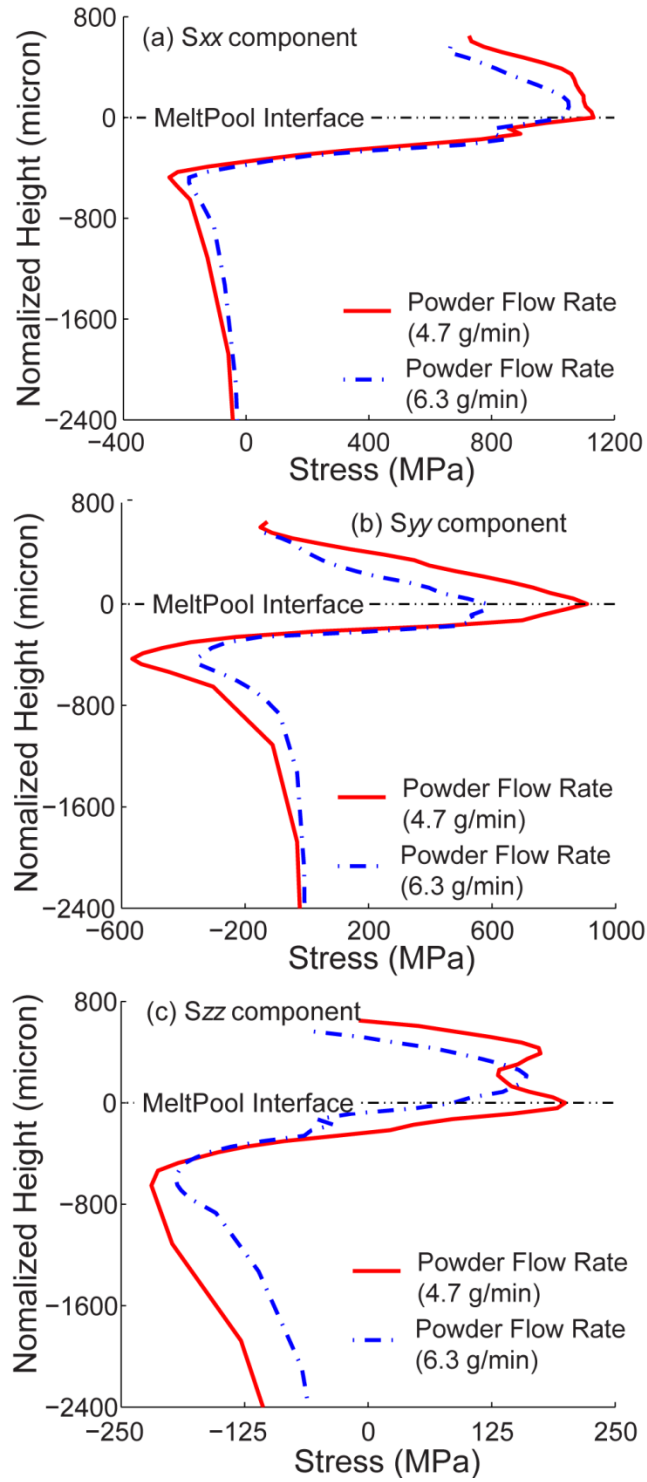


Figure 4.1 Residual stresses along the Z axis with different powder flow rate (4.7 g/min to 6.3 g/min): (a) S_{xx} component (b) S_{yy} component (c) S_{zz} component (the dashed down arrow in Figure 2.17 shows the region where the residual stress profile is made)

4.3 Laser power

To explore the effects of laser power on the residual stress, laser power is varied and the residual stress profiles along the Z axis are plotted in Figure 4.2. An increase in the power leads to thicker melt pool and the melt pool height increases about 100 % from 600 to 800 Watts. Therefore, the study in this section includes both the effects of the energy density and the melt pool geometry, especially the penetration depth to the substrate, on the residual stress fields due to the dependence of the melt pool geometry on laser power. Figure 4.2 shows that an increase in laser power raises the magnitudes of the residual stress in all directions even though a higher laser power promotes a slower cooling rate during cooling [48], and the magnitude of the transverse stress is more influenced by laser power than that of the longitudinal residual stress. The peak tensile residual stress is found around the melt pool interface, as same as the study varying the penetration depth with different powder flow rate in the previous Section 4.2. However, the location of the maximum compressive stress moves toward the substrate with higher power. We can conclude from the first two studies that a higher laser power with the same amount of powder flow rate increases the magnitude of the residual stress in both tensile and compressive directions due to the deeper penetration depth and influences more material downward with greater energy density.

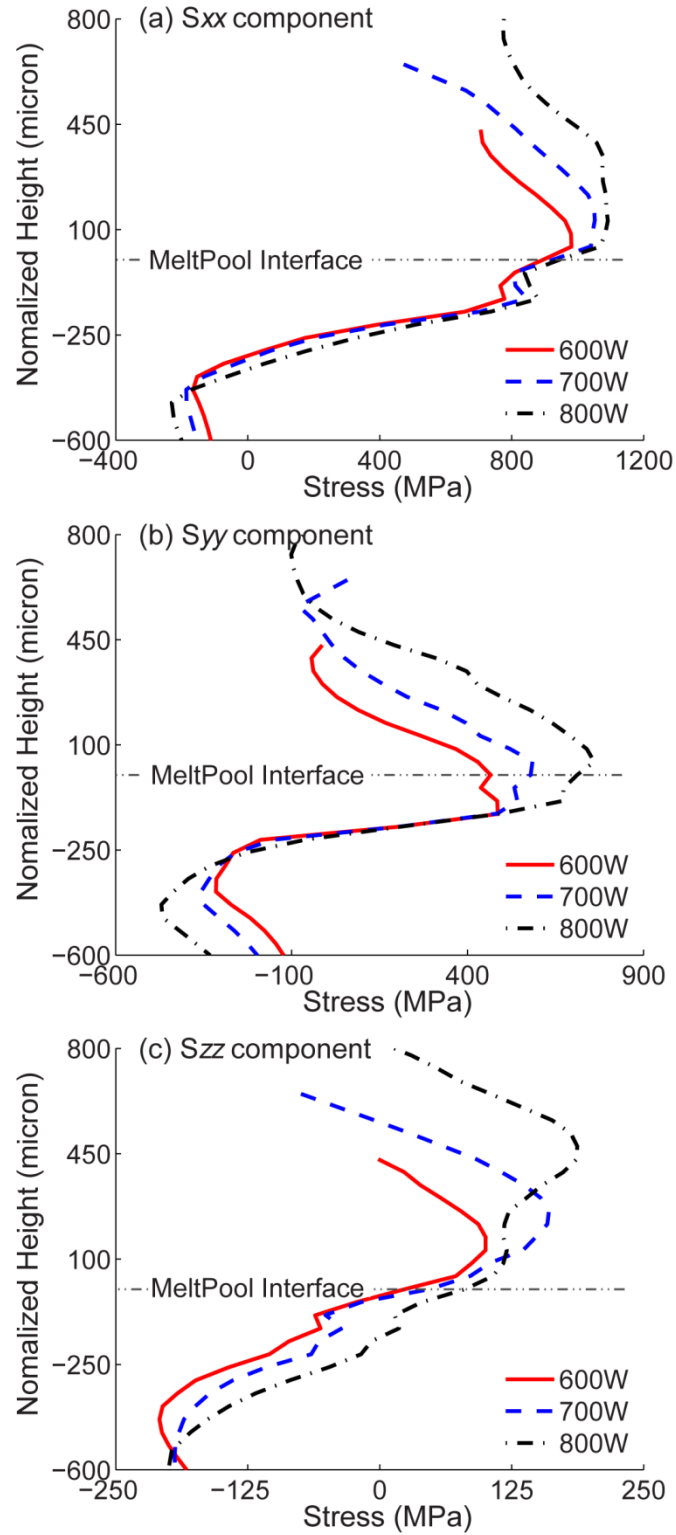


Figure 4.2 Residual stresses along the Z axis with different laser power (600 Watt to 800 Watt): (a) S_{xx} component (b) S_{yy} component (c) S_{zz} component (the dashed down arrow in Figure 2.17 shows the region where the residual stress profile is made)

4.4 Scanning speed

Figure 4.3 shows the residual stress distribution along the Z axis with the laser scanning speed from 8.5 (100 %) to 12.8 mm/s (150 %). Unlike the variation of the melt pool size with laser power, the melt pool height decreases only by 10 % with the fifty percent increase in the scanning speed; therefore, the main effects of cooling rate and energy density on the residual stress profile can be studied with minimizing the effects of the penetration depth. The maximum tensile stress is found around the melt pool interface with different scanning speed as the first two studies in Section 4.2 and 4.3, but the peak location of the compressive residual stress is raised up toward the top surface with less energy density by faster scanning speed. The magnitude of the residual stress in both tensile and compressive directions increases with scanning speed due to a rise in cooling rate with faster scanning speed [48] and the increase in the residual stress with 150 % of the scanning speed is relatively smaller than the increase caused by varying powder flow rate and laser power, which suggests that the penetration depth of the melted material to the substrate with different processing parameters is more effective to control the magnitude of the residual stress than cooling rate in DMD process.

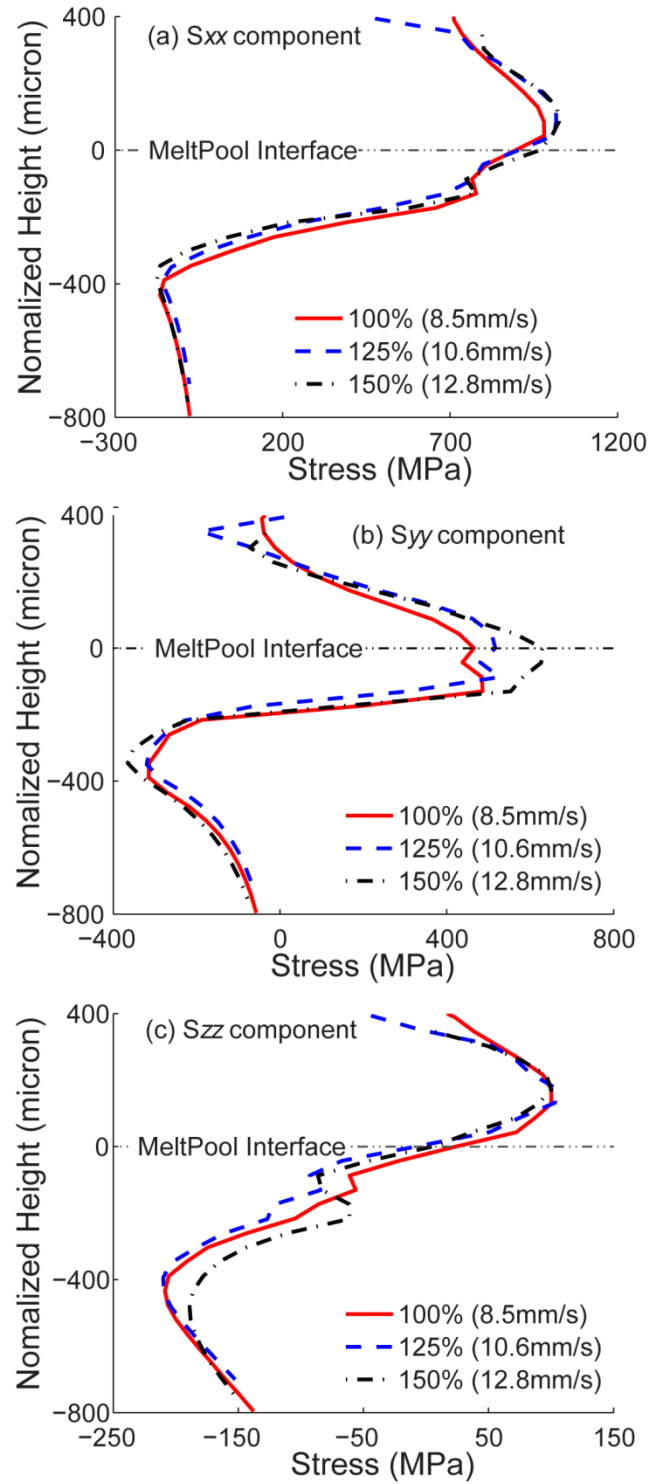


Figure 4.3 Residual stresses along the Z axis with different laser scanning speed (8.5 mm/s to 12.8 mm/s): (a) S_{xx} component (b) S_{yy} component (c) S_{zz} component (the dashed down arrow in Figure 2.17 shows the region where the residual stress profile is made)

4.5 Scanning direction / deposition layer thickness

Three different scanning techniques in the laser deposition of a 300 micron-height layer are introduced in this section as shown in Figure 4.4 and the residual stresses with the three different scanning techniques are compared to figure out the effects of scanning direction and the number of layers for a target deposition height on the residual stress.

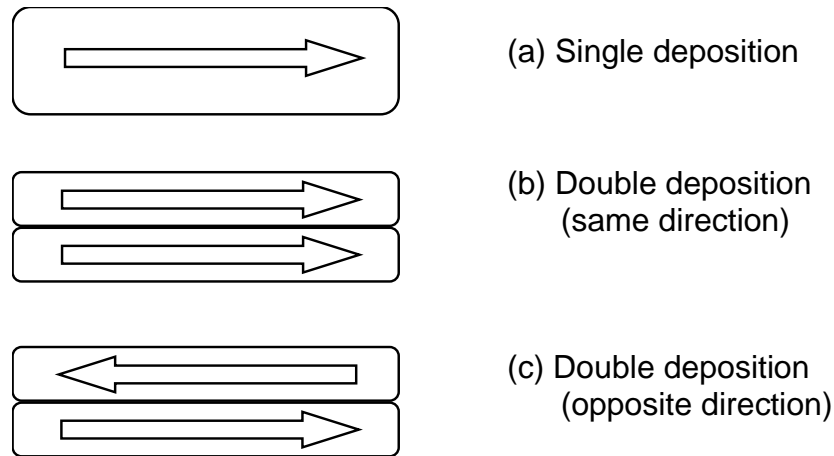


Figure 4.4 Different scanning techniques to investigate the effects of scanning direction and deposition layer thickness on the residual stress (target deposition height of 300 microns)

Figure 4.6 shows that the profile / magnitude of the residual stresses in the double 150 micron layer depositions with the opposite laser scanning direction for the second layer deposition are almost the same because the second layer experiences the same thermal loads in both cases as seen in Figure 4.5. However, the magnitudes of the tensile and compressive stresses in the normal directions increase and the locations of the peak stresses move downward into the bottom substrate with multiple thin layer depositions. To figure out how the second layer alters the stress distribution, transient stresses with

different scanning techniques (Figure 4.4 (a) and (b)) are compared in Figure 4.7. Two regions are chosen: one in tensile stress state (Figure 4.7 (a)) and another in compressive stress state (Figure 4.7 (b)) after the first layer deposition. Stress initially drops toward compressive direction as the laser beam is approaching due to the thermal expansion of the thermally affected neighboring layers and it rises back with cooling. Since the second layer is deposited before the material is fully cooled down to the ambient temperature, which is the common condition in real DMD production, the rise in stress by contraction during cooling in the first thin layer deposition is smaller than that in the thick single layer deposition. Another reason for the lesser rise during cooling is the smaller amount of solidified / cooled material in the thinner layer deposition. With laser thermal loads from the second thin layer deposition, stress again drops toward compressive direction, and the amounts of drop during heating stage are about the same for both the first and the second thin layer depositions. However, the initial state of the stress is different: in the first layer deposition, the material has zero state stress, but the material in the second layer deposition has the residual stress built in the first layer deposition. Therefore, if the initial stress state of the first layer is in tensile as in Figure 4.7 (a) case, the residual stress after the second layer deposition is accumulated in tensile direction and it is greater than the stress formed in the first layer deposition. The residual stress in Figure 4.7 (b) case is also accumulated in compressive direction by the second layer deposition. Due to the fact that the residual stress is added up with each layer deposition, a single 300 micron layer deposition gives the least amount of the residual stress among the three different cases. We can conclude from this study that the least magnitudes of the residual stress in both tensile and compressive directions with better quality of deposition (least penetration

depth) can be achieved by providing higher energy density with optimizing the interacting time with a target material, which eventually leads to the highest deposition rate.

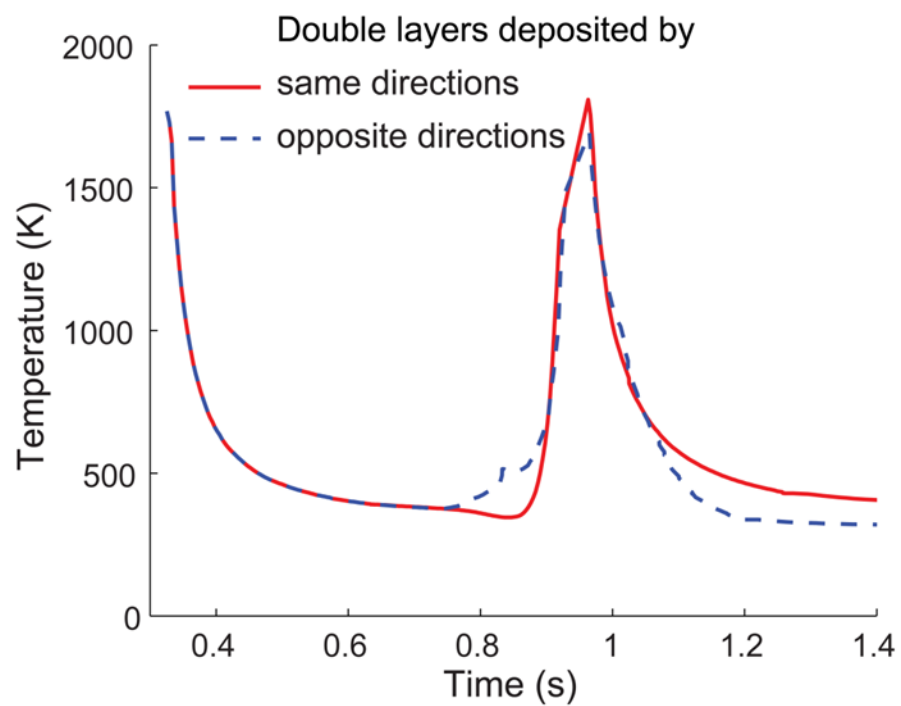


Figure 4.5 Temperature history of double layer deposition with different scanning directions

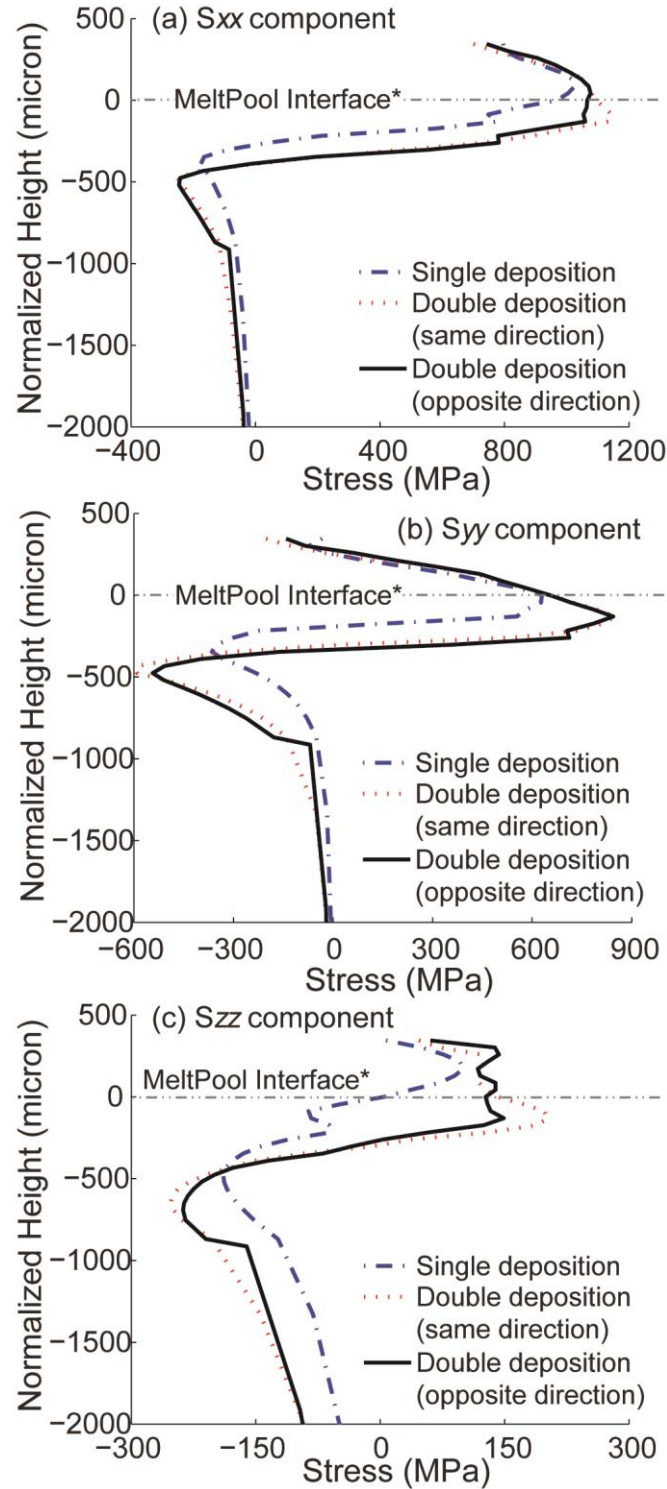


Figure 4.6 Residual stresses along the Z axis with different scanning direction and layer thickness (See Figure 4.4): (a) S_{xx} component (b) S_{yy} component (c) S_{zz} component (the dashed down arrow in Figure 2.17 shows the region where the residual stress profile is made)

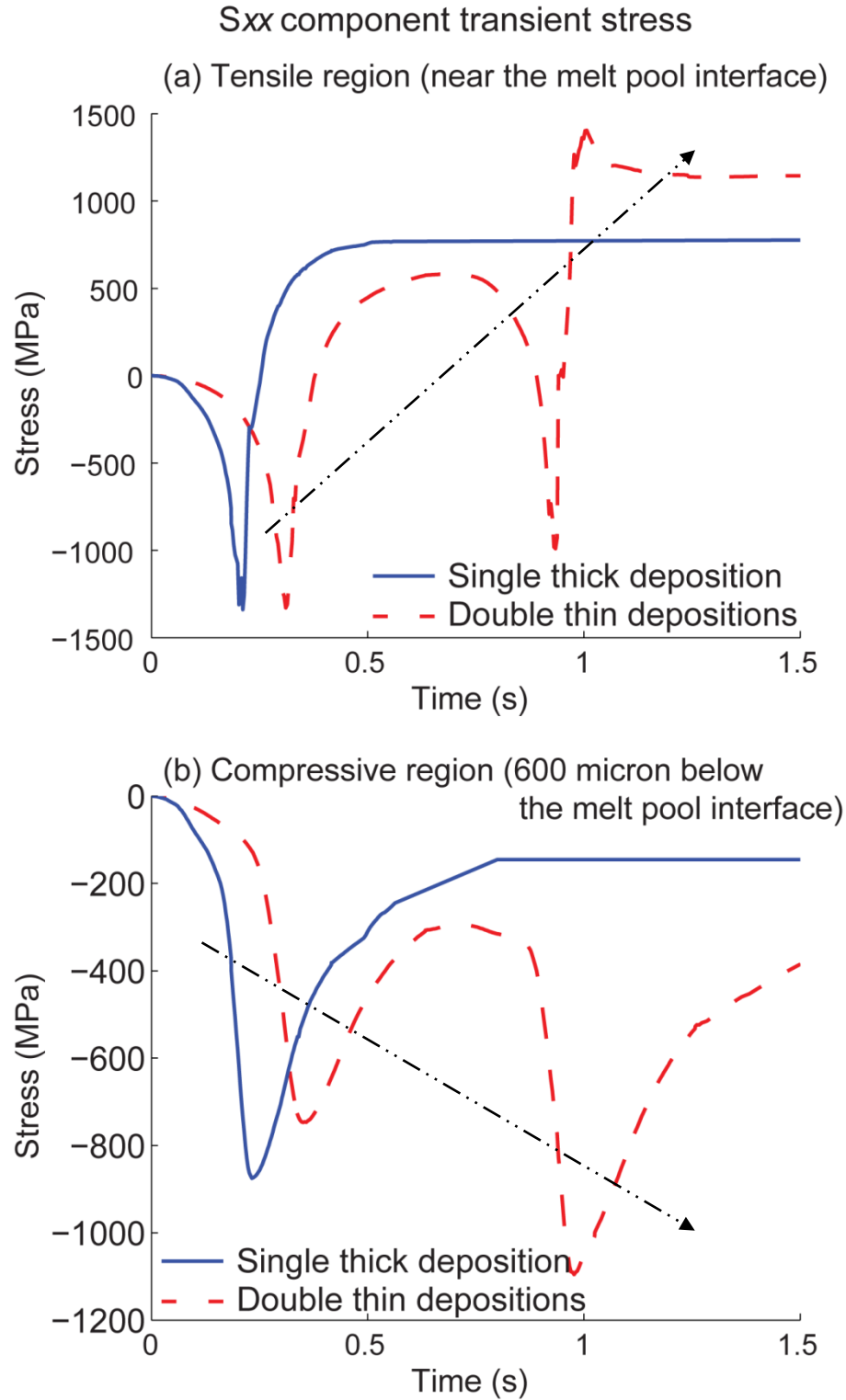


Figure 4.7 Transient stress with the different number of scanings in 300 micron height deposition of AISI 4340 steel: (a) tensile region (close to the melt pool interface) (b) compressive region (600 micron below the interface) after the first layer deposition

4.6 Conclusions

In this Chapter, the experimentally validated mathematical models described in Chapter II and III are utilized to investigate the effects of the processing variables on the residual stress in DMD process. The important conclusions are provided below.

- 1) The peak tensile residual stress is always found around the melt pool interface with different processing parameters (powder flow rate, laser power, and scanning speed).
- 2) The melt pool height is independent on powder flow rate if energy density is constrained, but powder flow rate changes the penetration depth to the substrate. An increase in the penetration depth with lower powder flow rate raises the magnitudes of the residual stress in both tensile and compressive directions because deeper penetration restores more the compressive stress formed by thermal expansion of the thermally affected material during heating stage.
- 3) The melt pool penetration to the substrate is the most dominant factor to determine the magnitude of the residual stress among energy density, cooling rate, melt pool size, and melt pool location.
- 4) The residual stress profile along the Z axis is governed by the amount of energy density: the higher the energy density, the deeper the region the residual stress exists.
- 5) Faster cooling rate with increased scanning speed leads to an increase in the residual stress, but the amount of increase is less significant than the increase by varying laser power and powder flow rate.

- 6) The magnitudes of the residual stress in both tensile and compressive directions are greater in double thin layer depositions than a single thick layer deposition due to the accumulation of the residual stress formed by the first layer deposition.
- 7) The least magnitudes of the residual stress in tensile and compressive directions with better quality of deposition (least penetration depth) can be achieved by providing higher energy density with optimizing the interacting time with a target material, which eventually leads to the highest deposition rate.

CHAPTER V

CONTRIBUTIONS AND FUTURE WORKS

5.1 Contributions

This dissertation presents the numerical and experimental analyses of residual stress evolution in in low alloy steel in laser aided Direct Metal Deposition (DMD) process. Specifically this study has the following contributions:

- 1) To improve accuracy of the previous mathematical thermal model in DMD process, non-equilibrium partitioning in solidification process and the modified solute transport equation are adapted. Due to the hyperbolic differential equations, the second order CFL condition is also used to optimize time step and mesh size for convergence.
- 2) To reduce tremendous computational time, the calculations are parallelized using OpenMp to be run by a computer cluster.
- 3) Due to a number of alloying elements in AISI 4340 steel, two sub-binary systems (carbon-iron and nickel-iron) are chosen to determine the state of material and to investigate the solute transport of carbon and nickel in liquid iron solution.
- 4) Different laser type and mode are added in the mathematical model and powder temperature profiles with different conditions are predicted, which provides the

optimal laser mode and powder distribution for better control of melt pool temperature.

- 5) Since martensitic phase transformation exists in AISI 4340 steel laser deposition and it has a significant effect on the residual stress, martensitic phase volume phase is calculated using empirical relationships.
- 6) Thermal model is experimentally validated by comparing temperature, fluid flow, and the geometry change with laser power. Temperature is monitored by an infrared pyrometer and the flow velocity at the melt pool surface is calculated from successive melt pool images taken by a high speed CCD camera. With improved accuracy, the numerical results agree with the experimental measurements.
- 7) Mechanical deformation model in DMD process considering solid state phase transformation and thermal loads from a laser heat source is built using commercial software package ABAQUS with user subroutines.
- 8) Mechanical deformation model is validated by X-ray diffraction residual stress measurement.
- 9) The evolution of residual stress is analyzed using the mathematical model and dependence of residual stress on melt pool size / location is found. Due to the dependence, the residual stress can be controlled by altering melt pool geometry with providing different processing parameters.
- 10) The processing parameters, such as powder flow rate, scanning speed, laser power, scanning direction, and deposition thickness, are varied to investigate the effects of processing variables on the residual stress. The most significant factor to

determine the magnitudes of the residual stress is the penetration depth to the substrate and the second most significant parameter is the energy density used in the process. The energy density also plays important role to define the residual stress profile along the Z axis. Lastly, a single thick layer deposition with minimal penetration provides the least amount of the residual stress and the most efficient deposition with higher quality.

5.2 Future works

Laser aided Direct Metal Deposition process is one of intelligent and innovative manufacturing system to build a complex metallic shape with a feedback control of geometry, temperature, composition, and metallurgical phase. Since DMD process involves sequence of heating and melting and it has a number of processing variables, an understanding of physical phenomena in DMD process through a series of experiments requires tremendous time and costs. In this study, a mathematical model has been used to investigate the important physical phenomena during laser material interaction and to obtain the correlations between processing variables and the thermal / mechanical behaviors of the material. However, the computational cost is currently high due to the capability of the current CPUs for multi-physics calculations although a parallelized computing OpenMp is adapted in the models. To increase the computational speed, we will adapt another type of parallelism, such as task parallelism, in the model. Then, the faster computing speed will allow us to predict the overall residual stress profile in a small block deposition as shown in Figure 5.1 and to investigate the correlations between laser scanning parameters / techniques and the residual stress, so that we can predict the controllable range of the residual stress with a given material type and shape. The post-

heating with a defocused beam followed by a number of deposition layers will also be included in the analysis: a defocused beam size / power and the suitable heat treatment layer thickness for minimal tooling time. Since the typical DMD product has a complex geometry, such as a conformal cooling channel in injection mold for example, various geometries will be case studied as seen in Figure 5.2 to examine how the product geometry influences the residual stress and how the residual stress can be controlled. Lastly, a dimensional analysis will be conducted from the obtained correlations with several case studies to provide a number to estimate the residual stress field and how many layers before the post-heating by defocused beam is necessary to recover the mechanical deformation. Dimensionless numbers will also be built by the laser processing parameters (laser power, scanning speed, and powder flow rate), material properties (thermal diffusivity, CTE, and flow stress), metallurgical phase, and geometry (size and shape).

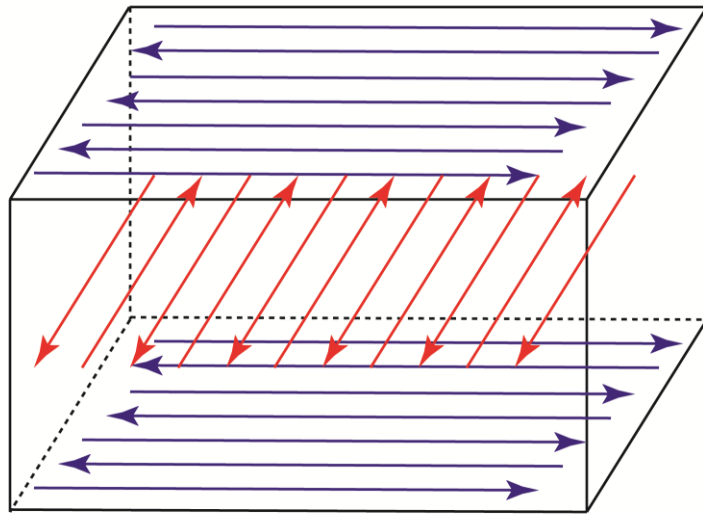


Figure 5.1 Zigzag pattern laser scanning for a single block fabrication

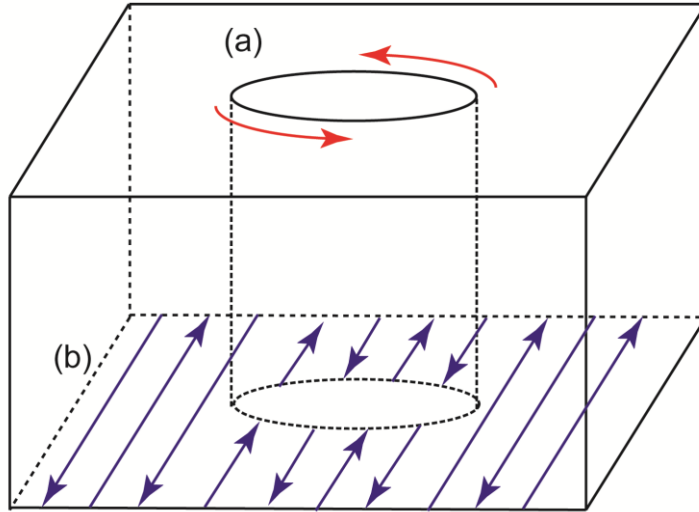


Figure 5.2 Different scanning direction in laser aided metal deposition of a block with a hole: (a) circular scanning (b) one by one scanning

BIBLIOGRAPHY

- [1] Mazumder J, Qi H. Fabrication of 3-D components by laser aided direct metal deposition. In: Schriempf JT, editor. Critical Review: Industrial Lasers and Applications, vol. 5706. 2005. p.38.
- [2] Hoadley AFA, Rappaz M. A thermal-model of laser cladding by powder injection. Metall Mater Trans B 1992;23:631.
- [3] Picasso M, Marsden CF, Wagniere JD, Frenk A, Rappaz M. A simple but realistic model for laser cladding. Metall Mater Trans B 1994;25:281.
- [4] Kelly SM, Kampe SL. Microstructural evolution in laser-deposited multilayer Ti-6Al-4V builds: Part II. Thermal modeling. Metall Mater Trans A 2004;35A:1869.
- [5] Toyserkani E, Khajepour A, Corbin S. Three-dimensional finite element modeling of laser cladding by powder injection: Effects of powder feedrate and travel speed on the process. J Laser Appl 2003;15:153.
- [6] Costa L, Vilar R, Reti T, Deus AM. Rapid tooling by laser powder deposition: Process simulation using finite element analysis. Acta Mater 2005;53:3987.
- [7] Zheng B, Zhou Y, Smugeresky JE, Schoenung JM, Lavernia EJ. Thermal behavior and microstructural evolution during laser deposition with laser-engineered net shaping: Part I. Numerical calculations. Metall Mater Trans A 2008;39A:2228.

- [8] Kahlen FJ, Kar A. Residual stresses in laser-deposited metal parts. *J Laser Appl* 2001;13:60.
- [9] Deus AM, Mazumder J. Two-dimensional thermo-mechanical finite element model for laser cladding. In: Duley W, Shibata K, Poprawe R, editors. *Proceedings of ICALEO*. Orlando (FL): Laser Institute of America, 1996. p.B174.
- [10] Vasinonta A, Beuth JL, Griffith M. Process maps for predicting residual stress and melt pool size in the laser-based fabrication of thin-walled structures. *J Manuf Sci Eng - Trans ASME* 2007;129:101.
- [11] Dai K, Shaw L. Thermal and stress modeling of multi-material laser processing. *Acta Mater* 2001;49:4171.
- [12] Ghosh S, Choi J. Three-dimensional transient finite element analysis for residual stresses in the laser aided direct metal/material deposition process. *J Laser Appl* 2005;17:144.
- [13] Ghosh S, Choi J. Modeling and experimental verification of transient/residual stresses and microstructure formation in multi-layer laser aided DMD process. *J Heat Transf -Trans Asme* 2006;128:662.
- [14] Ghosh S, Choi J. Deposition pattern based thermal stresses in single-layer laser aided direct material deposition process. *J Manuf Sci Eng - Trans ASME* 2007;129:319.
- [15] Qi H, Mazumder J, Ki H. Numerical simulation of heat transfer and fluid flow in coaxial laser cladding process for direct metal deposition. *J Appl Phys* 2006;100.
- [16] He X, Mazumder J. Transport phenomena during direct metal deposition. *J Appl Phys* 2007;101.

- [17] Yang YS, Na SJ. A study on residual stresses in laser surface hardening of a medium carbon steel. *Surf Coat Tech* 1989;38:311.
- [18] Pape JA, Neu RW. A comparative study of the fretting fatigue behavior of 4340 steel and PH 13-8 Mo stainless steel. *Int J Fatigue* 2007;29:2219.
- [19] Bennon WD, Incropera FP. A continuum model for momentum, heat and species transport in binary solid-liquid phase change systems—II. Application to solidification in a rectangular cavity. *Int J Heat Mass Transf* 1987;30:2171.
- [20] Bennon WD, Incropera FP. A continuum model for momentum, heat and species transport in binary solid-liquid phase change systems—I. Model formulation. *Int J Heat Mass Transf* 1987;30:2161.
- [21] Bennon WD, Incropera FP. Numerical Analysis of Binary Solid-Liquid Phase Change Using a Continuum Model. *Numer Heat Transf B* 1988;13:277.
- [22] Incropera FP, Engel AHH, Bennon WD. Numerical analysis of binary solid-liquid phase change with buoyancy and surface tension driven convention. *Numer Heat Transf A* 1989;16:407.
- [23] Prakash C, Voller V. On the numerical solution of continuum mixture model equations describing binary solid-liquid phase change. *Numer Heat Transf B* 1989;15:171.
- [24] Military handbook - MIL-HDBK-5H: Metallic materials and elements for aerospace vehicle structures (Knovel Interactive Edition). U.S. Department of Defense. p.2.

- [25] Fisher DJ. Data compilation diffusion in ferrous alloys: Stafa-Zuerich: Trans Tech., 2006.
- [26] Bramson MA. Infrared radiation. A handbook for applications. New York: Plenum Press: Optical Physics and Engineering, 1968.
- [27] Singh R, Alberts MJ, Melkote SN. Characterization and prediction of the heat-affected zone in a laser-assisted mechanical micromachining process. *Int J Mach Tool Manu* 2008;48.
- [28] Qui TQ, Longtin JP, Tien CL. Characteristics of radiation absorption in metallic particles. *J Heat Tranf* 1995;117.
- [29] Tolochko NK, Laoui T, Khlopkov YV, Mozzharov SE, Titov VI, Ignatiev MB. Absorptance of powder materials suitable for laser sintering. *Rapid Prototyping Journal* 2000;6:155.
- [30] He X, Yu G, Mazumder J. Temperature and composition profile during double-track laser cladding of H13 tool steel. *J Phys D Appl Phys* 2010;43.
- [31] Osher S, Sethian JA. Front propagating with curvature-dependent speed: algorithms based on hamilton-jacobi formulations. *J of Comput Phys* 1988;79:12.
- [32] Ki H. Modeling and measurement of processes with liquid-vapor interface created by high power density lasers. Mechanical Engineering, vol. Ph. D.: University of Michigan, 2001.
- [33] Kar A, Mazumder J. Model for nonequilibrium partitioning during rapid solidification of binary concentrated-solutions. *Acta Metall* 1992;40:1873.

- [34] Ki H, Mohanty PS, Mazumder J. Modeling of laser keyhole welding: Part II. Simulation of keyhole evolution, velocity, temperature profile, and experimental verification. *Metall Mater Trans A* 2002;33A:1831.
- [35] Bailey NS, Tan W, Shin YC. Predictive modeling and experimental results for residual stresses in laser hardening of AISI 4140 steel by a high power diode laser. *Surf Coat Tech* 2009;203:2003.
- [36] Gray GT, Chen SR, Wright W, Lopez MF. Constitutive equations for annealed metals under compression at high strain rates and high temperatures. In: Wing P, editor: Los Alamos National Laboratory, 1994.
- [37] Inoue T. *Metallo - thermomechanics - application to quenching*. Materials Park, OH 44073-0002, USA: ASM International, Member/Customer Service Center, 2002.
- [38] Rohde U, Jeppsson A. Literature review of heat treatment simulations with respect to phase transformation, residual stresses and distortion. *Scand J Metall* 2000;29:47.
- [39] Ju DY, Zhang WM, Zhang Y. Modeling and experimental verification of martensitic transformation plastic behavior in carbon steel for quenching process. *Mat Sci Eng a-Struct* 2006;438:246.
- [40] Brooks CR. *Principles of the heat treatment of plain carbon and low alloy steels*: ASM International, 1996.
- [41] Bhattacharya S, Dinda GP, Dasgupta AK, Mazumder J. Microstructural evolution of AISI 4340 steel during Direct Metal Deposition process. *Mater Sci Eng A* 2011;528:2309.

- [42] Pappas N, Watkins TR, Cavin OB, Jaramillo RA, Ludtka GM. Retained austenite in SAE 52100 steel post magnetic processing and heat treatment. In: Han Q, Ludtka GM, Zhai Q, editors. *Materials Processing under the Influence of External Fields: The Minerals, Metals terials Society*, 2007. p.37.
- [43] Koistinen DP, Marburger RE. A general equation prescribing the extent of the austenite-martensite transformation in pure iron-carbon alloys and plain carbon steels. *Acta Metall* 1959;7:59.
- [44] Andrews K. Empirical formulae for the calculation of some transformation temperatures. *J Iron Steel Inst* 1965;203:721.
- [45] Avrami M. Kinetics of phase change I - General theory. *J Chem Phys* 1939;7:1103.
- [46] Fernandes FMB, Denis S, Simon A. Mathematical model coupling phase transformation and temperature evolution during quenching of steels. *Mater Sci Tech* 1985;1.
- [47] Prevey PS. Use of pearson VII distribution functions in X-ray diffraction residual stress measurement. *Adv X Ray Anal* 1986;29:103.
- [48] Mazumder J, Steen WM. Heat transfer model for cw laser material processing. *J Appl Phys* 1980;51:941.